Physics-informed recovery of nonlinear residual stress fields in an inverse continuum framework

José A. Sanz-Herrera[a,*], Alain Goriely[b]

[a]*Escuela Técnica Superior de Ingeniería, Universidad de Sevilla*
[b]*Mathematical Institute, University of Oxford*

Abstract

Residual stresses play a critical mechanical role in both industrial and biomechanical applications. In biological tissues, residual stresses arise from growth and remodeling processes under physiological or pathological conditions and have been extensively modeled within the framework of nonlinear elasticity. These modeling efforts have enabled direct computation of residual stress patterns based on phenomenological growth laws. However, experimental validation and feedback for these models remain limited due to the inherent challenges in measuring complex stress distributions. To address this limitation, we propose and develop an inverse approach for estimating nonlinear residual stresses using information from an externally loaded configuration. Specifically, the algorithm employs domain displacement fields and externally applied loads as input data, which can be experimentally obtained through biaxial testing and digital image correlation (DIC) techniques. This novel formulation and numerical scheme are rooted in a physics-informed continuum framework that enforces universal principles of mechanics. To evaluate the framework, a synthetically generated ground-truth solution serves as a reference, allowing assessment of the accuracy of residual stress field reconstruction across varying levels of noise in the input data. Performance metrics indicate a significant improvement in reconstruction accuracy when multiple load cases and combined datasets are

---

[*]Corresponding author. Camino de los descubrimientos s/n, 41092 Seville, Spain. Tel.: +34 954 486079; fax: +34 954 487295

Email address: `jsanz@us.es` (José A. Sanz-Herrera)

used. This approach paves the way for the formulation of growth laws and residual patterns based on experimental data.

Keywords: Residual stress, inverse methods, tissue mechanics, biomechanics, nonlinear mechanics, finite element method

---

1. Introduction

The concept of *residual stress* is generically used to define an initially (pre)-stressed configuration in the elasticity boundary value problem, referred to a preloaded reference or initial configuration. By definition, it is the stress in a material in the absence of external loads or body forces [1, p. 39]. The term ‘residual’ refers to internal physical process which motivates the appearance of such a pre-stressed state. These stresses in industrial applications are typically unwanted and the result of a rapid cooling or quenching process in which stresses do not have time to fully relax before the material becomes a solid. The most extreme case of such stresses is found in Prince Rupert’s drop where residual stresses transform a material to give it both extreme strength and extreme fragility [2].

Yet, residual stresses play an important mechanical role both in industrial and biophysical applications. The most popular sources of residual stresses in metallic materials are due to manufacturing and fabrication processes, such as joining techniques, i.e. welding, and surface treatments [3–5]. Although such residual stresses usually have negative mechanical implications, they are known to improve mechanical resistance against fatigue of alloys [6, 7].

In biology, since the seminal work of Fung [8], residual stresses are known to be crucial to the proper function of tissues and organs and are precisely tuned and maintained through life (see [1] for examples in bacterial, fungal, plant, animal, and physiological systems). Therefore, significant effort has been dedicated to investigating the origins of residual stresses in biological tissues, understanding their biophysical roles, and unraveling the complexities of these stress states to establish their connection to physiological (mechanobiological) functions [9–12]. There is a vast literature dedicated to the investigation of residual stress patterns as a consequence of a growth process in soft biological tissues, and their corresponding continuum modeling and numerical finite element development [13–16]. Residual stresses have been investigated in growing skin [17, 18], growing tumors [19–21] biological membranes [22–24], tendons [25, 26], brain tissue [27, 28] and their abnormalities [29], cardiovascular tissues [30–38] and associated pathologies [39, 40] such as hypertension [41]. The impact of residual stresses has also been explored in bone (hard) tissue biomechanics [42].

The bulk of the studies about residual stresses provide either modeling techniques or numerical approaches to the problem but are mostly restricted to direct (or *forward*) methodologies, in which residual stress patterns can be computed in tissues after calibration of model parameters. However, the accuracy and usefulness of these direct approaches depend on the availability and quality of data to fit phenomenological laws of growth/remodeling. The most popular method to experimentally quantifying residual stresses in arteries is the opening angle test, and was introduced more than three decades ago [43, 44]. Since then, this assay and others have been used to estimate uniform pre-stresses to be used as an input data in growth of cardiovascular tissue models [34, 45–48]. However, direct measurement of nonuniform residual stress patterns or their validation through models have not been reported in the literature. The goal of this article is to develop *inverse* techniques to infer the residual stress field from experimental measurements.

Inverse methods in continuum mechanics aim at computing complex spatial distributions of variables and parameters which are usually assumed to be known in direct boundary value problems. In the field of biomechanics, inverse methods have been applied to compute traction forces by cells in artificial substrates [49–55], to reconstruct stiffness patterns in degradable matrices [56], and to map stiffness in tissues (i.e. elastography) [57] and cells [58–60]. A variety of inverse formulations and applications, incorporating constraints and/or regularization, have been proposed in the literature [61, 62]. However, to the best of the authors' knowledge, no studies have yet addressed residual stress following the inverse modeling statements used in the referred works.

Inverse techniques typically require the measurement of domain displacement fields as an input data. Remarkably, nowadays this information can be routinely obtained in tissues by means, for instance, of Digital Image Correlation (DIC). DIC is an enabling methodology to map displacement fields and has been used, among others, in abominal aorta [63], skin [64], and bone tissue [65, 66]. Interestingly, DIC data were used in a mixed computational-experimental approach to estimate 3D residual stress fields in arteries [67].

In this paper we present, for the first time, an inverse approach for quantifying complex nonlinear residual stress patterns. The formulation is designed to search an initial residual stress state, established in a continuum framework, through the imposition of universal principles (i.e. physics-informed) in two configurations, namely: reference and externally loaded configurations. The continuum equations are numerically elaborated resulting in a two-steps algorithm. As far as we know, both the formulation and the numerical scheme are novel. Although this initial study is motivated by the recovery of residual stresses in tissues, and hence limited to 2D cases by DIC, the same framework can also be applied to 3D and applications found in industry if the data is available.

The paper is organized as follows. Section 2 presents the rationales and preliminaries of the study, including the feasibility of reconstructing complex nonlinear residual stresses. Section 3 develops the continuum inverse formulation as well as the numerical discretization, linearization and solver algorithm. Section 4 describes the case for analysis, and shows and discusses results of inverse reconstruction of variables and associated errors versus a ground truth solution. Finally, some conclusions are drawn at the end of the paper.

2. Background

We first review the nonlinear formulation of residual stresses at (elastic) finite strains. Although the proposed inverse formulation is not restricted to any particular source of residual stresses, the presented examples of application will consider that residual stresses are the consequence of an internal growth process. Formally, the same analysis holds for *any* anelastic process. The feasibility of recovering residual stresses in nonlinear solids using an externally loaded configuration is also demonstrated.

2.1. Nonlinear modeling of residual stresses

We assume that residual stresses are the result of an internal nonlinear and inhomogeneous growth process, characterized by a deformation gradient tensor $\boldsymbol{F}^g$ defined in an initial domain $\mathcal{B}_I$ (see Figure 1). After growth, a residual stress state $\boldsymbol{\sigma}^0$ usually arises as a phenomenological response to naturally circumvent the kinematic incompatibility of such a growth within the body. Indeed, the deformed configuration $\mathcal{B}_0$ can be kinematically decomposed via a stress-free and incompatible configuration $\mathcal{B}_0'$ (see Figure 1), such that $\boldsymbol{\sigma}^0 = \boldsymbol{\sigma}^0(\boldsymbol{F}^a)$, with $\boldsymbol{F}^a$ being the (assembly) deformation gradient tensor from the incompatible (stress-free) to the deformed (reference) configuration.

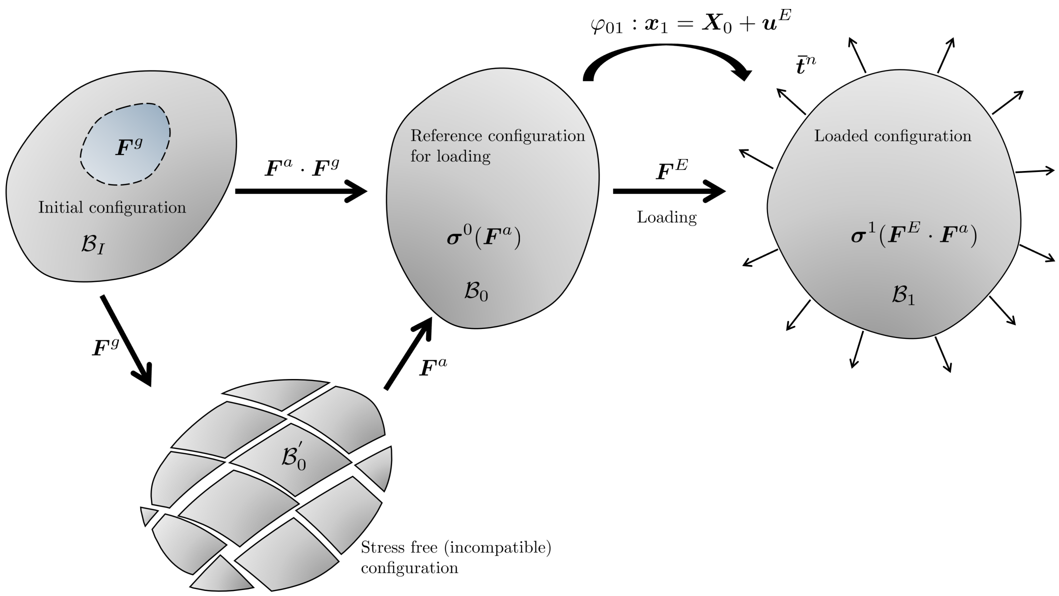

Figure 1: Schematics of the different configurations used in our formulation to recover non-linear residual stresses from an auxiliary and externally loaded configuration. We assume that residual stresses ($\boldsymbol{\sigma}^0$ in the reference configuration $\mathcal{B}_0$) are the result of an internal growth process, characterized by deformation gradient tensor $\boldsymbol{F}^g$ in an intial domain $\mathcal{B}_I$. On the other hand, the reference configuration can be kinematically decomposed through an incompatible configuration $\mathcal{B}_0'$ and assembled into configuration $\mathcal{B}_0$ by deformation gradient tensor $\boldsymbol{F}^a$. Finally, an additional externally loaded configuration $\mathcal{B}_1$ by boundary (Cauchy) traction vector $\bar{\boldsymbol{t}}^n$, and deformation gradient tensor $\boldsymbol{F}^E$, is established.

$\boldsymbol{F}^a$ does not arise from a real displacement field, although we will define after this displacement field numerically in our algorithmic development.

The right Cauchy-Green strain tensor $\mathbf{C}^a$, and the second Piola-Kirchhoff stress tensor $\mathbf{S}^0$ are defined as,

$$\mathbf{C}^a = \boldsymbol{F}^{a\top} \cdot \boldsymbol{F}^a, \qquad \mathbf{S}^0 = 2 \left[\frac{\partial \Psi(\mathbf{C})}{\partial \mathbf{C}} \right]_{\mathbf{C}=\mathbf{C}^a} . \tag{1}$$

Then, residual stresses in the reference configuration $\mathcal{B}_0$ (see Figure 1) are expressed as the push-forward of the second Piola-Kirchhoff stress tensor as follows:

$$\boldsymbol{\sigma}^0 = \frac{2}{J^a} \cdot \boldsymbol{F}^a \left[\frac{\partial \Psi(\mathbf{C})}{\partial \mathbf{C}} \right]_{\mathbf{C}=\mathbf{C}^a} \cdot \boldsymbol{F}^{a\top}, \tag{2}$$

with $J^a = \det(\boldsymbol{F}^a)$.

In order to recover residual stresses from the deformed configuration $\mathcal{B}_0$ after growth, using the inverse approach of Section 3, a loaded configuration $\mathcal{B}_1$ needs to be established and characterized. Indeed, we assume that data from external loading $\bar{\boldsymbol{t}}^n$ and kinematics field $\boldsymbol{u}^E$, i.e. mapping from $\mathcal{B}_0$ to $\mathcal{B}_1$ (see Figure 1), can be obtained using mechanical testing and DIC, as explained in [63]. We see $\bar{\boldsymbol{t}}^n$ and $\boldsymbol{u}^E$, the *data*, as input quantities in our algorithm (see Section 3). Then, the elastic deformation gradient $\boldsymbol{F}^E$ is defined as,

$$\boldsymbol{F}^E = \frac{\partial \boldsymbol{x}_1}{\partial \boldsymbol{X}_0} = \mathbf{I} + \frac{\partial \boldsymbol{u}^E}{\partial \boldsymbol{X}_0} \tag{3}$$

Finally, the Cauchy stress tensor $\boldsymbol{\sigma}^1$ in the loaded configuration (see Figure 1) can be analogously defined from Equations (1–2):

$$\boldsymbol{\sigma}^1 = \frac{2}{J^e} \cdot \boldsymbol{F}^e \left[\frac{\partial \Psi(\mathbf{C})}{\partial \mathbf{C}} \right]_{\mathbf{C}=\mathbf{C}^e} \cdot \boldsymbol{F}^{e\top} \tag{4}$$

with $\mathbf{C}^e = \boldsymbol{F}^{e\top} \cdot \boldsymbol{F}^e$, $\boldsymbol{F}^e = \boldsymbol{F}^E \cdot \boldsymbol{F}^a$ and $J^e = \det(\boldsymbol{F}^e)$.

In these expressions Ψ is a given hyper-elastic strain-energy density function. We assume in our study an incompressible neo-Hookean behavior of the form

$$\Psi(\mathbf{C}) = \frac{\mu}{2}(I_1 - 3) \tag{5}$$

where I_1 is the first invariant (trace), of the right Cauchy-Green deformation tensor $\mathbf{C}$. μ is the shear modulus.

2.2. Proof of concept

Our goal is to propose an inverse recovery of residual stresses using, as input data, information about boundary applied loads and body motion from a reference to a loaded configuration. We demonstrate in this section the feasibility of our approach.

As a proof of concept, we consider an unconfined solid with a circular region of interest (ROI), which undergoes a growth process limited to the ROI domain (Figure 2a). The elastic response of the material is modeled by a hyperelastic incompressible neo-Hookean law (Figure 2b) and growth is modeled using an isotropic but inhomogeneous deformation gradient tensor $\boldsymbol{F}^g$ following, in the initial domain, a sigmoid function as shown in Figure 2c. The growth problem is solved using the finite element (FE) software Abaqus Simulia. Then, from the initial configuration (Figure 3a) we obtain

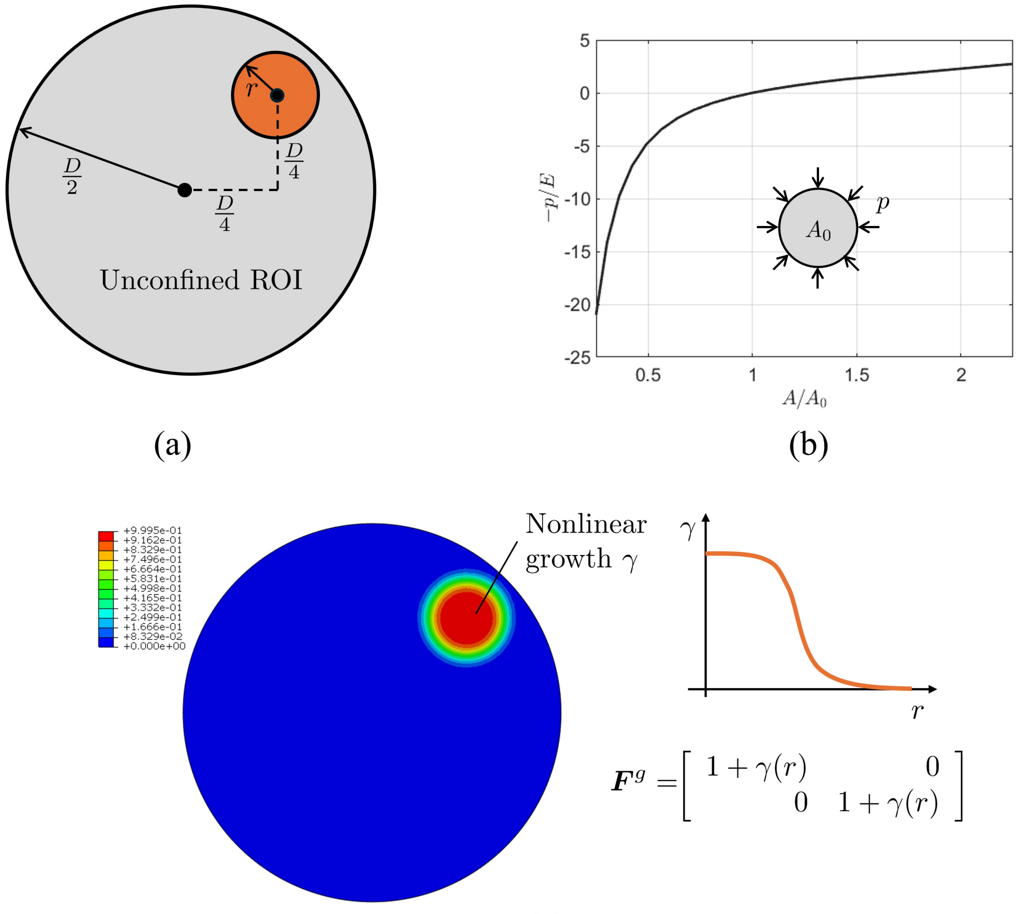

(a) (b)

(c)

Figure 2: Proof-of-concept example. (a) A nonlinear and inhomogeneous growth process is induced at the orange location within an unconfined ROI of diameter D. The solid is modeled as a hyperelastic plane-stress incompressible body. (b) Constitutive neo-Hookean model representing dimensionless pressure p/E (E being the Young's modulus) versus surface change from reference area A_0. (c) Growth is spatially modeled by a deformation gradient tensor $\boldsymbol{F}^g$ using a nonlinear function (γ) centered at $(D/4, D/4)$ with an exponential decay according to a sigmoid function. Colors represent the values of γ in the ROI.

a deformed configuration with a residual stress state after growth represented in Figure 3b. Using this prestressed body as a reference configuration, an external elastic deformation is applied to obtain a new loaded configuration.

The strain state of this loaded configuration is shown in Figure 3c both assuming a linear and nonlinear material behavior. Interestingly, differences in the strain field can be observed when the nonlinear model is loaded from a pre-stressed configuration versus a stress-free one. However, no differences are found in the strain field, being independent of the initial stress state, when using a linear model. Therefore, residual stress recovery from a loaded and deformed configuration is limited to solids that show a nonlinear constitutive behavior. In fact, as far as input displacement fields are usually noisy, the efficiency of inverse algorithms improves as the differences between these strain patterns increase versus a reference one [60].

3. Inverse physics-informed recovery of residual stresses

We now give details on our inverse physics-informed formulation for the recovery of residual stress patterns. The mathematical description is split into the continuum formulation, finite element (FE) numerical discretization, linearization, and solver algorithm.

3.1. Continuum formulation

We assume a known reference configuration ($\mathcal{B}_0$ in Figure 1) subjected to an unknown residual stress state $\boldsymbol{\sigma}^0$. To unravel such a stress field, a known (measured) external load ($\bar{\boldsymbol{t}}^n$ in Figure 1) is applied in order to get a loaded configuration ($\mathcal{B}_1$ in Figure 1). The motion from the reference to the loaded configuration is characterized by the displacement field $\boldsymbol{u}^E$ (Figure 1). In practice, this field may be obtained by DIC methods, for instance. We assume that the measurement of this displacement field is noisy. Hence, we rename this (noisy) quantity to $\boldsymbol{u}^{E\star}$. Both $\bar{\boldsymbol{t}}^n$ and $\boldsymbol{u}^{E\star}$ are input data in our formulation. Note that the problem, as stated, is independent on the source of the residual stress state.

In our formulation we search for the closest displacement field $\boldsymbol{u}^E$ to the measured one $\boldsymbol{u}^{E\star}$ together with the residual stress field $\boldsymbol{\sigma}^0$, while satisfying fundamental physical principles such as compatibility and equilibrium conditions, in both the reference and loaded configurations. In the absence of

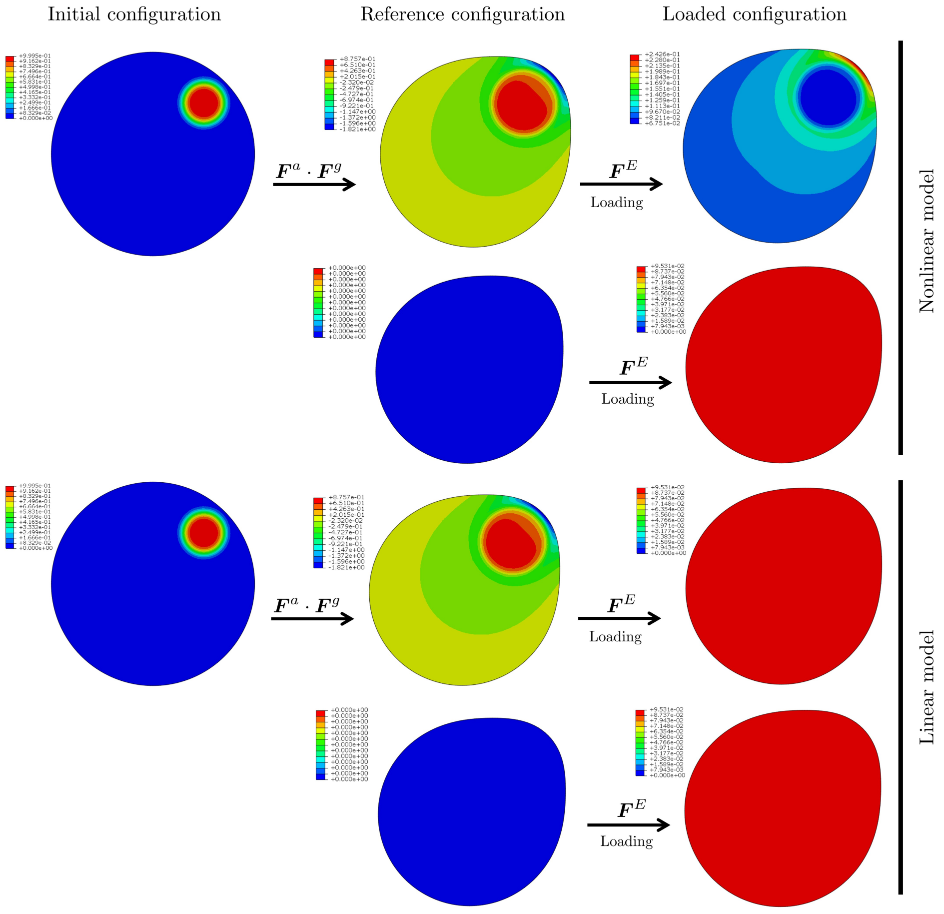

(a) (b) (c)

Figure 3: Results of the proof of concept example shown in Figure 2. (a) Initial configuration ($\mathcal{B}_I$ in Figure 1) and growth, according to the problem stated in Figure 2. (b) Deformed configuration after growth ($\mathcal{B}_0$ in Figure 1), showing residual (dimensionless) hydrostatic pressure distribution (normalized versus E). Also, a null residual stress state is considered in the second row. (c) First principal component of the logarithmic strain tensor in the loaded configuration ($\mathcal{B}_1$ in Figure 1), after applying a $0.1 \cdot D$ normal displacement on the boundary (D being the diameter of the ROI in the initial configuration). The strain measure is shown for a nonlinear (neo-Hookean) and linear material modeling, when loading in the reference configuration from both pre-stressed and stress-free conditions.

body forces, this condition can be mathematically expressed, as

$$\underset{\boldsymbol{\sigma}^0, \boldsymbol{u}^E}{\operatorname{argmin}} \quad \frac{1}{2}||\boldsymbol{u}^E - \boldsymbol{u}^{E\star}||_2^2 + \frac{\lambda}{2}\int_{\mathcal{B}_0} ||\nabla_0 \boldsymbol{\sigma}^0||_2^2 \mathrm{d}v, \tag{6}$$

$$s.t.$$

$$\nabla_0 \times \boldsymbol{F}^a = \boldsymbol{0}, \quad \nabla_0 \cdot \boldsymbol{\sigma}^0 = \boldsymbol{0} \quad \in \mathcal{B}_0, \quad \boldsymbol{\sigma}^0 \cdot \boldsymbol{n}^0 = \boldsymbol{0} \quad \in \Gamma_{\mathcal{B}_0} \tag{7}$$

$$\nabla_1 \times \boldsymbol{F}^E = \boldsymbol{0}, \quad \nabla_1 \cdot \boldsymbol{\sigma}^1 = \boldsymbol{0} \quad \in \mathcal{B}_1, \quad \boldsymbol{\sigma}^1 \cdot \boldsymbol{n}^1 = \bar{\boldsymbol{t}}^n \quad \in \Gamma_{\mathcal{B}_1}, \tag{8}$$

where $\boldsymbol{n}^0$ and $\boldsymbol{n}^1$ are the outward normals to $\mathcal{B}_0$ and $\mathcal{B}_1$, respectively. The second term in Eq. (6) represents a $L-1$ (Thikhonov) regularization term which penalizes non-smooth stress fields, with a regularization parameter λ. This parameter will be calibrated in our study following the $L-$curve criterion [68]. The stress fields $\boldsymbol{\sigma}^0$ and $\boldsymbol{\sigma}^1$ are obtained from a hyperelastic strain energy density function, according to Eqs. (2) and (4), respectively.

Note that physical equilibrium and compatibility conditions are imposed in a strong form in the continuum framework shown in (7–8). For convenience, we also express these conditions in a weak form, using the principle of virtual work to obtain

$$\underset{\boldsymbol{\sigma}^0,\boldsymbol{u}^E}{\operatorname{argmin}} \quad \frac{1}{2}||\boldsymbol{u}^E - \boldsymbol{u}^{E\star}||_2^2 + \frac{\lambda}{2}\int_{\mathcal{B}_0} ||\nabla_0 \boldsymbol{\sigma}^0||_2^2 \mathrm{d}v \tag{9}$$

$$s.t.$$

$$\mathcal{W}^0(\boldsymbol{\sigma}^0, \delta\boldsymbol{u}^0) = \int_{\mathcal{B}_0} \boldsymbol{\sigma}^0 \cdot \delta\boldsymbol{\varepsilon}^0 \mathrm{d}v = 0 \tag{10}$$

$$\mathcal{W}^1(\boldsymbol{u}^E, \boldsymbol{\sigma}^0, \delta\boldsymbol{u}^1) = \int_{\mathcal{B}_1} \boldsymbol{\sigma}^1(\boldsymbol{u}^E, \boldsymbol{\sigma}^0) \cdot \delta\boldsymbol{\varepsilon}^1 \mathrm{d}v - \int_{\Gamma_{\mathcal{B}_1}} \bar{\boldsymbol{t}}^n \cdot \delta\boldsymbol{u}^1 \mathrm{d}s = 0, \tag{11}$$

$\mathcal{W}^0$ represents the virtual work (spatial version) developed by real internal stress $\boldsymbol{\sigma}^0$ with virtual strain field $\delta\boldsymbol{\varepsilon}^0$ in the reference configuration $\mathcal{B}_0$. On the other hand, $\mathcal{W}^1$ represents the virtual work (spatial version) developed by real internal stress $\boldsymbol{\sigma}^1$ and external boundary tractions $\bar{\boldsymbol{t}}^n$ with virtual strain $\delta\boldsymbol{\varepsilon}^1$ and displacement $\delta\boldsymbol{u}^1$ fields, respectively, in the loaded configuration $\mathcal{B}_1$. The strain fields $\delta\boldsymbol{\varepsilon}^0$ and $\delta\boldsymbol{\varepsilon}^1$ are compatible (virtual) fields with virtual displacement fields $\delta\boldsymbol{u}^0$ and $\delta\boldsymbol{u}^1$ through the following relation [69]:

$$\delta\boldsymbol{\varepsilon}^K = \frac{1}{2}\left(\nabla_K \delta\boldsymbol{u}^K + \nabla_K^\top \delta\boldsymbol{u}^K\right), \qquad K = 0, 1. \tag{12}$$

Note that due to the the absence of external forces in (10) and hence the absence of external virtual work, the residual stress field must be self-balanced in the reference configuration. The internal and external virtual works must be identical as seen in Eqs. (10–11). Therefore, the virtual fields $\delta\boldsymbol{u}^0$, $\delta\boldsymbol{u}^1$ (and corresponding fields $\delta\boldsymbol{\varepsilon}^0(\delta\boldsymbol{u}^0)$, $\delta\boldsymbol{\varepsilon}^1(\delta\boldsymbol{u}^1)$ in Eqs. (10)-(11) through Eq. (12)) can be interpreted as Lagrangian multiplier fields, and included in the cost function (9) as follows:

$$\underset{\boldsymbol{\sigma}^0,\boldsymbol{u}^E}{\operatorname{argmin}} \quad \frac{1}{2}||\boldsymbol{u}^E-\boldsymbol{u}^{E\star}||_2^2+\frac{\lambda}{2}\int_{\mathcal{B}_0}||\nabla_0\boldsymbol{\sigma}^0||_2^2\mathrm{d}v+\mathcal{W}^0(\boldsymbol{\sigma}^0,\delta\boldsymbol{u}^0)+\mathcal{W}^1(\boldsymbol{u}^E,\boldsymbol{\sigma}^0,\delta\boldsymbol{u}^1). \tag{13}$$

3.2. FE discretization and numerical scheme

The continuum fields $\boldsymbol{u}^E$, $\boldsymbol{u}^{E\star}$, $\boldsymbol{\sigma}^0$, $\delta\boldsymbol{u}^0$ and $\delta\boldsymbol{u}^1$ are discretized and interpolated within each FE element as $\boldsymbol{u}^E \approx \mathbf{N}_u^1 \cdot \mathbf{u}_i^E$, $\boldsymbol{u}^{E\star} \approx \mathbf{N}_u^1 \cdot \mathbf{u}_i^{E\star}$, $\boldsymbol{\sigma}^0 \approx \mathbf{N}_\sigma^0 \cdot \boldsymbol{\sigma}_i^0$, $\delta\boldsymbol{u}^0 \approx \mathbf{N}_u^0 \cdot \delta\mathbf{u}_i^0$ and $\delta\boldsymbol{u}^1 \approx \mathbf{N}_u^1 \cdot \delta\mathbf{u}_i^1$. $\mathbf{u}_i^E$, $\mathbf{u}_i^{E\star}$, $\boldsymbol{\sigma}_i^0$, $\delta\mathbf{u}_i^0$ and $\delta\mathbf{u}_i^1$ are discrete node-valued vectors, which contains the components of each (discrete) variable at the nodes i of the element. $\mathbf{N}_u^0$, $\mathbf{N}_u^1$ and $\mathbf{N}_\sigma^0$ are the corresponding shape (interpolating) functions within the element referred to their corresponding reference (0) or loaded (1) discrete configurations. Using (12) together with the defined discretized quantities yields $\delta\boldsymbol{\varepsilon}^0 \approx \mathbf{B}_u^0\cdot\delta\mathbf{u}_i^0$ and $\delta\boldsymbol{\varepsilon}^1 \approx \mathbf{B}_u^1 \cdot \delta\mathbf{u}_i^1$, with $\mathbf{B}_u^0$ and $\mathbf{B}_u^1$ being the gradient matrices of interpolating shape function matrices $\mathbf{N}_u^0$ and $\mathbf{N}_u^1$ of the element in the discretized reference and loaded configurations, respectively [70, 71]. Using this discretization and introducing it in (13) yields:

$$\underset{\boldsymbol{\sigma}^0,\mathbf{u}^E}{\operatorname{argmin}} \quad \phi \tag{14}$$

with

$$\phi = \frac{1}{2}\sum_{k=1}^{NE}(\mathbf{u}_i^E-\mathbf{u}_i^{E\star})^\top\cdot(\mathbf{u}_i^E-\mathbf{u}_i^{E\star})+$$
$$+\frac{\lambda}{2}\sum_{k=1}^{NE}\left(\int_{\mathcal{B}_{0,k}}(\mathbf{B}_\sigma^0\cdot\boldsymbol{\sigma}_i^0)^\top\cdot(\mathbf{B}_\sigma^0\cdot\boldsymbol{\sigma}_i^0)\mathrm{d}v\right)+\mathcal{W}^0(\boldsymbol{\sigma}_i^0,\delta\mathbf{u}_i^0)+\mathcal{W}^1(\mathbf{u}_i^E,\boldsymbol{\sigma}_i^0,\delta\mathbf{u}_i^1), \tag{15}$$

where $\mathbf{B}_\sigma^0$ is the gradient matrix of interpolating shape function matrix $\mathbf{N}_\sigma^0$ of the element k in the reference (discretized) configuration $\mathcal{B}_{0,k}$. NE is the number of elements of the FE mesh. In addition, we have

$$\mathcal{W}^0(\boldsymbol{\sigma}^0,\delta\boldsymbol{u}^0)=\sum_{k=1}^{NE}\left(\int_{\mathcal{B}_{0,k}}(\boldsymbol{\sigma}_k^0\cdot\mathbf{B}_u^0\mathrm{d}v)^\top\cdot\delta\mathbf{u}_i^0\right)=(\mathbf{F}^{\mathrm{int},0})^\top\cdot\delta\mathbf{u}^0, \tag{16}$$

and

$$\begin{aligned}\mathcal{W}^1(\boldsymbol{u}_i^E, \boldsymbol{\sigma}_i^0, \delta\boldsymbol{u}_i^1) &= \sum_{k=1}^{NE}\left(\int_{\mathcal{B}_{1,k}} (\boldsymbol{\sigma}_k^1 \cdot \mathbf{B}_u^1 \mathrm{d}v)^\top \cdot \delta\mathbf{u}_i^1 - \int_{\Gamma_{\mathcal{B}_{1,k}}} (\mathbf{N}_u^1 \cdot \mathbf{T}^n ds)^\top \cdot \delta\mathbf{u}_i^1\right)\\ &= (\mathbf{F}^{\text{int},1} - \mathbf{F}^{\text{ext},1})^\top \cdot \delta\mathbf{u}^1,\end{aligned} \tag{17}$$

where $\mathbf{T}^n$ is the discretized boundary traction vector in the loaded configuration in Eq (17). $\mathbf{F}^{\text{int},0}$, $\mathbf{F}^{\text{int},1}$ and $\mathbf{F}^{\text{ext},1}$ are internal and external global vectors of forces, after FE assembly, in Eqs. (16–17) [70, 71]. Finally, after FE assembly Eq. (15) yields

$$\begin{aligned}\phi = \quad & \frac{1}{2}(\mathbf{u}^E - \mathbf{u}^{E\star})^\top \cdot (\mathbf{u}^E - \mathbf{u}^{E\star}) + \frac{\lambda}{2}(\tilde{\mathbf{B}}_\sigma^0 \cdot \boldsymbol{\sigma}^0)^\top \cdot (\tilde{\mathbf{B}}_\sigma^0 \cdot \boldsymbol{\sigma}^0)\\ & \qquad\qquad\qquad + (\mathbf{F}^0)_{\text{int}}^\top \cdot \delta\mathbf{u}^0 + (\mathbf{F}_{\text{int}}^1 - \mathbf{F}_{\text{ext}}^1)^\top \cdot \delta\mathbf{u}^1,\end{aligned} \tag{18}$$

where $\mathbf{u}^E$, $\mathbf{u}^{E\star}$, $\boldsymbol{\sigma}^0$, $\delta\mathbf{u}^0$ and $\delta\mathbf{u}^1$ are node-valued global vectors which contain the components of the variables at each FE node of the mesh. $\tilde{\mathbf{B}}_\sigma^0$ is the global gradient matrix after assembly of element matrices $\mathbf{B}_\sigma^0$.

Eq. (14) has a minimum stationary solution at $\delta\phi(\mathbf{u}^E, \boldsymbol{\sigma}^0, \delta\mathbf{u}^0, \delta\mathbf{u}^1) = \mathbf{0}$. Hence, using (16–18),

$$\begin{aligned}&\frac{\partial\phi}{\partial\mathbf{u}^E} = \mathbf{0} \rightarrow \mathbf{u}^E - \mathbf{u}^{E\star} + \frac{\partial\mathcal{W}^1}{\partial\mathbf{u}^E} = \mathbf{0} \rightarrow\\ &\rightarrow \mathbf{u}^E - \mathbf{u}^{E\star} + \frac{\partial\mathbf{F}^{\text{int},1}}{\partial\mathbf{u}^E} \cdot \delta\mathbf{u}^1 - \frac{\partial\mathbf{F}^{\text{ext},1}}{\partial\mathbf{u}^E} \cdot \delta\mathbf{u}^1 = \mathbf{0}\end{aligned} \tag{19}$$

$$\begin{aligned}&\frac{\partial\phi}{\partial\boldsymbol{\sigma}^0} = \mathbf{0} \rightarrow \lambda\tilde{\mathbf{B}}_\sigma^{0\top} \cdot \tilde{\mathbf{B}}_\sigma^0 \cdot \boldsymbol{\sigma}^0 + \frac{\partial\mathcal{W}^0}{\partial\boldsymbol{\sigma}^0} + \frac{\partial\mathcal{W}^1}{\partial\boldsymbol{\sigma}^0} = \mathbf{0} \rightarrow\\ &\rightarrow \lambda\tilde{\mathbf{B}}_\sigma^{0\top} \cdot \tilde{\mathbf{B}}_\sigma^0 \cdot \boldsymbol{\sigma}^0 + \frac{\partial\mathbf{F}^{\text{int},0}}{\partial\boldsymbol{\sigma}^0} \cdot \delta\mathbf{u}^0 + \frac{\partial\mathbf{F}^{\text{int},1}}{\partial\boldsymbol{\sigma}^0} \cdot \delta\mathbf{u}^1 = \mathbf{0}\end{aligned} \tag{20}$$

$$\frac{\partial\phi}{\partial\delta\mathbf{u}^1} = \mathbf{0} \rightarrow \frac{\partial\mathcal{W}^1}{\partial\delta\mathbf{u}^1} = \mathbf{0} \rightarrow \mathbf{F}^{\text{int},1} - \mathbf{F}^{\text{ext},1} = \mathbf{0} \tag{21}$$

$$\frac{\partial\phi}{\partial\delta\mathbf{u}^0} = \mathbf{0} \rightarrow \frac{\partial\mathcal{W}^0}{\partial\delta\mathbf{u}^0} = \mathbf{0} \rightarrow \mathbf{F}^{\text{int},0} = \mathbf{0} \tag{22}$$

The equations above give the gradient of ϕ. They can be summarized as follows,

$$\begin{aligned}&\delta\phi(\mathbf{u}^E, \boldsymbol{\sigma}^0, \delta\mathbf{u}^0, \delta\mathbf{u}^1) = \mathbf{0}\\ &\quad\rightarrow \left\{\begin{array}{c} \mathbf{u}^E - \mathbf{u}^{E\star} + \frac{\partial\mathbf{F}^{\text{int},1}}{\partial\mathbf{u}^E}\cdot\delta\mathbf{u}^1 - \frac{\partial\mathbf{F}^{\text{ext},1}}{\partial\mathbf{u}^E}\cdot\delta\mathbf{u}^1 \\ \lambda\tilde{\mathbf{B}}_\sigma^{0\top}\cdot\tilde{\mathbf{B}}_\sigma^{0}\cdot\boldsymbol{\sigma}^0 + \frac{\partial\mathbf{F}^{\text{int},0}}{\partial\boldsymbol{\sigma}^0}\cdot\delta\mathbf{u}^0 + \frac{\partial\mathbf{F}^{\text{int},1}}{\partial\boldsymbol{\sigma}^0}\cdot\delta\mathbf{u}^1 \\ \mathbf{F}^{\text{int},1} - \mathbf{F}^{\text{ext},1} \\ \mathbf{F}^{\text{int},0} \end{array}\right\} = \left\{\begin{array}{c}\mathbf{0}\\ \mathbf{0}\\ \mathbf{0}\\ \mathbf{0}\end{array}\right\}\end{aligned} \tag{23}$$

Eq. (23) is a set of nonlinear equations which can be linearized by using a Newton-Raphson procedure or, alternatively, it can be solved using iterative solvers such as L-BFGS in other inverse applications [57, 60, 72]. However, both procedures require the evaluation of complex tangent matrices, such as $\frac{\partial\mathbf{F}^{\text{int},1}}{\partial\boldsymbol{\sigma}^0}$. To circumvent this issue, a two-step algorithm is proposed and elaborated in the next section.

3.3. Linearization and algorithmic scheme

To demonstrate the power of the the mathematical formulation presented in previous sections, we consider the case of biaxially loaded samples. Importantly, the numerical approach can be adapted to other load setups with minor changes.

The reference and biaxially loaded configurations are discretized as shown in Figure 4. An incompatible stress-free configuration is also used in the proposed numerical scheme. This configuration is numerically built using the FE element mesh of the reference and loaded configurations with duplicated nodes.

First step

Equations (19) and (21) are first linearized and subsequently analyzed numerically as an initial step. We collect and adapt these equations together

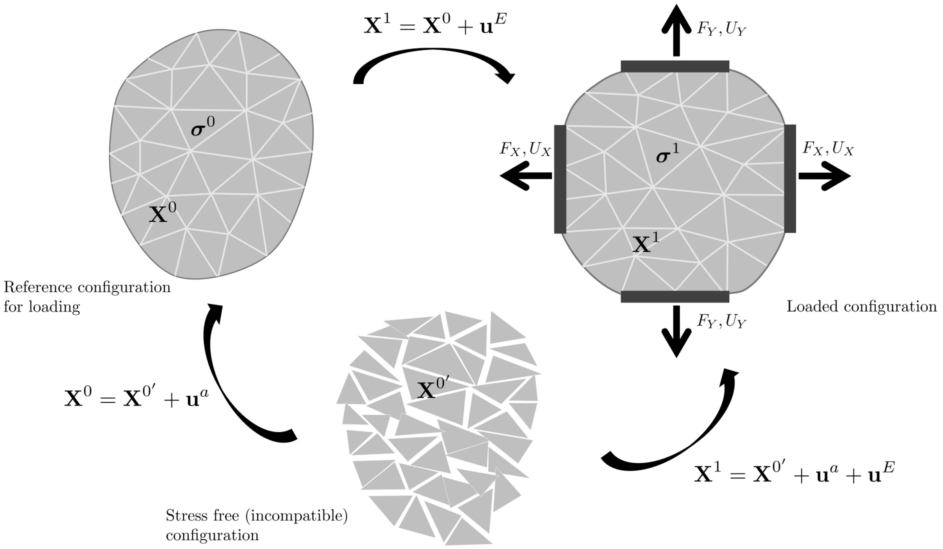

Figure 4: Discretized reference, loaded and stress-free (incompatible) configurations. An initial residual stress state $\boldsymbol{\sigma}^0$ is present in the elements of the reference configuration. Biaxial test input data F_X, U_X, F_Y, U_Y apply on the nodes at the location of the grips. Displacement (discrete) input vector $\mathbf{u}^E$ might be obtained by means of DIC techniques. The stress-free configuration is numerically built using the FE mesh of the reference and loaded configurations with duplicated nodes. $\mathbf{X}^0, \mathbf{X}^1$ and $\mathbf{X}^{0'}$ are vectors that contain the coordinates of the FE mesh of the reference, loaded and stress-free configurations, respectively.

with the biaxial load conditions as follows,

$$\mathbf{u}^E_\ell - \mathbf{u}^{E\star}_\ell + \left[\frac{\partial \mathbf{F}^{\text{int},1}}{\partial \mathbf{u}^E}\right]_\ell \cdot \delta \mathbf{u}^1_\ell = \mathbf{0} \tag{24}$$

$$\mathbf{F}^{\text{int},1}_\ell = \mathbf{0} \tag{25}$$

$$\left[\mathbf{u}^E_{N_{X-}}\right]_\ell = \mathbf{U}_{X^-}|_\ell, \quad \left[\mathbf{u}^E_{N_{X+}}\right]_\ell = \mathbf{U}_{X^+}|_\ell \tag{26}$$

$$\left[\mathbf{u}^E_{N_{Y-}}\right]_\ell = \mathbf{U}_{Y^-}|_\ell, \quad \left[\mathbf{u}^E_{N_{Y+}}\right]_\ell = \mathbf{U}_{Y^+}|_\ell \tag{27}$$

$$\sum_{i=1}^{nN_{X-}} \left[\mathbf{F}^{\text{ext},1}_i\right]_\ell = F_X|_\ell, \quad \sum_{i=1}^{nN_{X+}} \left[\mathbf{F}^{\text{ext},1}_i\right]_\ell = F_X|_\ell \tag{28}$$

$$\sum_{i=1}^{nN_{Y-}} \left[\mathbf{F}^{\text{ext},1}_i\right]_\ell = F_Y|_\ell, \quad \sum_{i=1}^{nN_{Y+}} \left[\mathbf{F}^{\text{ext},1}_i\right]_\ell = F_Y|_\ell, \tag{29}$$

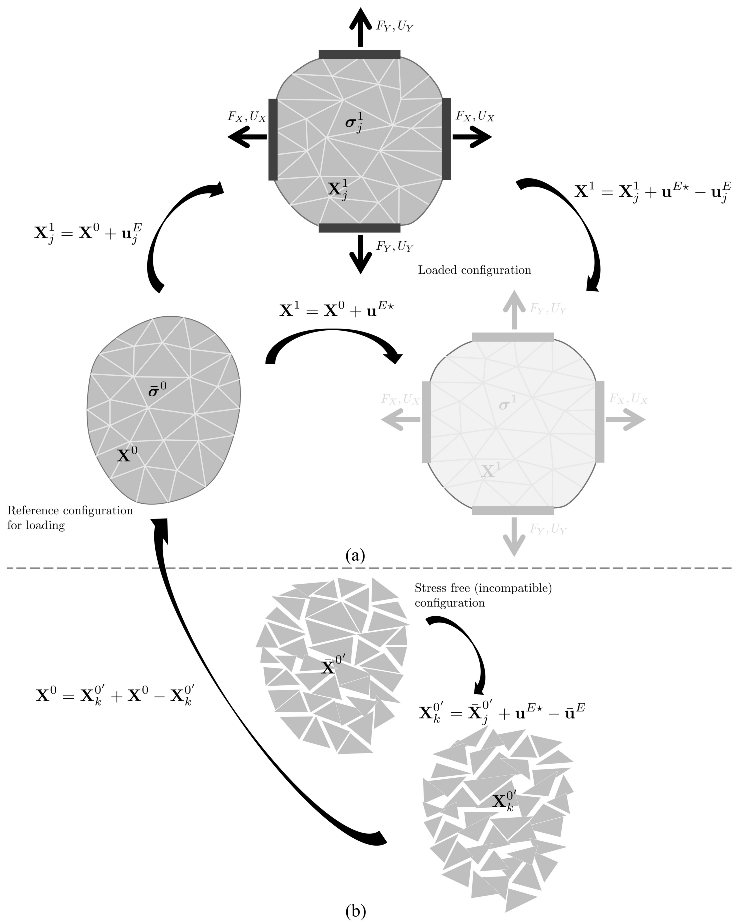

Figure 5: Two-step solver algorithm for a fixed load case. (a) First step: $\mathbf{u}_j^E$ is iteratively solved from pre-stressed configuration $\mathbf{X}^0$. $\bar{\boldsymbol{\sigma}}^0$ represents a previously converged residual stress vector of the second step algorithm (see overall numerical scheme in Box 1). The noisy configuration from measured noisy displacements $\mathbf{u}^{E\star}$ can be seen in shadows. (b) Second step: Incompatible mesh $\mathbf{X}_k^{0'}$ is obtained by applying the motion $\mathbf{u}^{E\star} - \bar{\mathbf{u}}^E$, $\bar{\mathbf{u}}^E$ obtained after convergence in the first step algorithm (a), to a previously converged stress-free configuration $\bar{\mathbf{X}}^{0'}$ (see overall numerical scheme in Box 1). Then $\bar{\boldsymbol{\sigma}}^0$ is obtained in the reference configuration $\mathbf{X}^0$ following the numerical scheme indicated in Box 1.

In biaxial tests combined with DIC, it is routine to obtain multiple stacks of data corresponding to different load cases, for instance, those including in a displacement loading ramp along the different axes. Therefore, $\left[\mathbf{u}^E_{N_{X-}}\right]_\ell$,

$\left[\mathbf{u}^E_{N_{X+}}\right]_\ell$, $\left[\mathbf{u}^E_{N_{Y-}}\right]_\ell$ and $\left[\mathbf{u}^E_{N_{Y+}}\right]_\ell$, in Eqs. (26)-(27) contain the components of the displacement vector $\mathbf{u}^E_\ell$ for each load case ℓ at the FE nodes attached to the left, right, top and bottom loading grips (see Figure 4), and they must be equal (i.e. compatible) with the measured motion of the grips (for each load case ℓ) on these nodes through vectors $\mathbf{U}_X|_\ell$, $\mathbf{U}_Y|_\ell$. Moreover, Eqs. (28)-(29) impose the equilibrium of overall grip forces $F_X|_\ell$, $F_Y|_\ell$, for each load case ℓ, with the resultant external forces vector $\left[\mathbf{F}^{\text{ext},1}_i\right]_\ell$ on these nodes. Note that nonuniform nodal forces along the boundaries of the grips are therefore allowed in the formulation, this feature being typically present in real biaxial experiments. nN_{X^-}, nN_{X^+}, nN_{Y^-} and nN_{Y^+}, are the number of nodes attached the left, right, top and bottom loading grips (see Figure 4). As a result, Eqs. (24–29) have to be solved for each load case ℓ.

Eqs. (24) and (25) are linearized using a Newton-Raphson method as,

$$\begin{bmatrix} \mathbf{1} & \mathbf{K}^{1\top}(\mathbf{u}^E_j,\bar{\boldsymbol{\sigma}}^0) \\ \mathbf{K}^1(\mathbf{u}^E_j,\bar{\boldsymbol{\sigma}}^0) & \mathbf{0} \end{bmatrix}_\ell \cdot \begin{Bmatrix} \mathbf{u}^E_{j+1} \\ \delta\mathbf{u}^1_{j+1} \end{Bmatrix}_\ell = \begin{Bmatrix} \mathbf{u}^{E\star} \\ -\mathbf{F}^{\text{int},1}_j(\mathbf{u}^E_j,\bar{\boldsymbol{\sigma}}^0) + \mathbf{K}^1(\mathbf{u}^E_j,\bar{\boldsymbol{\sigma}}^0)\cdot\mathbf{u}^E_j \end{Bmatrix}_\ell, \tag{30}$$

where $\mathbf{K}^1$ is the FE tangent stiffness matrix of (11) evaluated at previous iteration step j for vector $\mathbf{u}^E_j$, and for a previously converged residual stress vector $\bar{\boldsymbol{\sigma}}^0$ at the last iteration of the second step algorithm (see Figure 5a and overall numerical scheme in Box 1). Note that as a simplification, the derivative of the tangent stiffness matrix has been neglected in (30) during the linearization of (24). Biaxial load conditions are introduced in (26–29). Other load conditions may be included just by substituting this set of equations by the specific boundary conditions at hand. Eqs. (26–29) are implemented in (30) by means of Lagrangian operators, as is done for prescribed displacements and forces in the FEM [71]. The iterative procedure in (30) terminates when the relative difference $||\mathbf{u}^E_{j+1}-\mathbf{u}^E_j||/||\mathbf{u}^E_j||$ falls below a predefined tolerance. It is important to note that Eq. (30) must be solved and fully converged for each load case ℓ.

Second step

Linearization of Eqs. (20) and (22) can be challenging, or at the very least intrusive, within a conventional finite element (FE) framework, as it requires the handling of highly unconventional matrices. As an alternative, we propose addressing and solving the following (continuum) problem with a second algorithm:

$$\underset{\boldsymbol{\sigma}^0}{\operatorname{argmin}} \quad \frac{1}{2}||\boldsymbol{\sigma}^0 - \hat{\boldsymbol{\sigma}}^0||_2^2 + \frac{\lambda}{2}\int_{\mathcal{B}_0} ||\nabla_0 \boldsymbol{\sigma}^0||_2^2 \mathrm{d}v \tag{31}$$

$$s.t.$$

$$\mathcal{W}^0(\boldsymbol{\sigma}^0, \delta \boldsymbol{u}^0) = \int_{\mathcal{B}_0} \boldsymbol{\sigma}^0 \cdot \delta \boldsymbol{\varepsilon}^0 \mathrm{d}v = 0, \tag{32}$$

where $\hat{\boldsymbol{\sigma}}^0$ represents a residual stress state originating from the motion of the stress-free (incompatible) configuration to the reference configuration (see Figure 4). Details about the computation of this quantity along the algorithm are given below. Equations (31) and (32) are discretized and processed in a manner analogous to the procedure outlined in Section 3.2. Subsequently,

$$(\boldsymbol{\sigma}^0 - \hat{\boldsymbol{\sigma}}^0)^\top \cdot (\boldsymbol{\sigma}^0 - \hat{\boldsymbol{\sigma}}^0) + \lambda \tilde{\mathbf{B}}_\sigma^{0\top} \cdot \tilde{\mathbf{B}}_\sigma^0 \cdot \boldsymbol{\sigma}^0 + \frac{\partial \mathbf{F}^{\mathrm{int},0}}{\partial \boldsymbol{\sigma}^0} \cdot \delta \mathbf{u}^0, = \mathbf{0} \tag{33}$$

$$\mathbf{F}^{\mathrm{int},0} = \mathbf{0}. \tag{34}$$

Eqs. (33–34) are linearized with respect to $\boldsymbol{\sigma}^0$ and $\delta \mathbf{u}^0$ using a Newton-Raphson method:

$$\begin{bmatrix} \mathbf{1} + \lambda \tilde{\mathbf{B}}_\sigma^{0\top} \cdot \tilde{\mathbf{B}}_\sigma^0 & \tilde{\mathbf{B}}_u^{0\top} \\ \tilde{\mathbf{B}}_u^0 & \mathbf{0} \end{bmatrix} \cdot \begin{Bmatrix} \boldsymbol{\sigma}_{k+1}^0 \\ \delta \mathbf{u}_{k+1}^0 \end{Bmatrix} = \begin{Bmatrix} \hat{\boldsymbol{\sigma}}_k^0 \\ \mathbf{0} \end{Bmatrix}, \tag{35}$$

where $\tilde{\mathbf{B}}_u^0$ is the global gradient matrix after assembly of element matrices $\mathbf{B}_u^0$ in (16). $\hat{\boldsymbol{\sigma}}_k^0$ is computed in the reference configuration $\mathbf{X}^0$ as a result of the motion from the incompatible mesh $\mathbf{X}_k^{0'}$ to $\mathbf{X}^0$ (see Figure 5b). Incompatible mesh $\mathbf{X}_k^{0'}$ is obtained by applying the motion $\mathbf{u}^{E\star} - \bar{\mathbf{u}}^E$, obtained after convergence in the first step algorithm, to a previously converged stress-free configuration $\bar{\mathbf{X}}^{0'}$ (see Figure 5b and overall numerical scheme in Box 1). Since Eq. (35) is linear, it is solved in a single step.

Box 1: Two-step algorithm for residual stress recovery.

```
0. Initialize variables:
        $\boldsymbol{\sigma}^0_{k=0} = \mathbf{0}$
        $\mathbf{u}^E_{j=0} = \mathbf{u}^{E\star}$
        $\bar{\boldsymbol{\sigma}}^0 = \boldsymbol{\sigma}^0_{k=0}$
        $\bar{\mathbf{X}}^{0'} = \mathbf{X}^0$

WHILE $||\boldsymbol{\sigma}^0_{k+1} - \boldsymbol{\sigma}^0_k||/||\boldsymbol{\sigma}^0_{k=0}|| < \mathrm{TOL}$
    FOR EACH LOAD CASE $\ell$
      1. First step
         WHILE $||\mathbf{u}^E_{j+1,\ell} - \mathbf{u}^E_{j,\ell}||/||\mathbf{u}^E_{j,\ell}|| < \mathrm{TOL}$
             Solve Eq. (30).
             $j \leftarrow j + 1$
         END WHILE
         Update variable $\bar{\mathbf{u}}^E_\ell = \mathbf{u}^E_{j,\ell}$
      2. Second step
             ■ Obtain $\mathbf{X}^{0'}_{k,\ell} = \bar{\mathbf{X}}^{0'} + \mathbf{u}^{E\star}_\ell - \bar{\mathbf{u}}^E_\ell$ (see Figure 5b) using
               converged $\bar{\mathbf{u}}^E_\ell$.
             ■ Apply the displacement field $\mathbf{X}^0 - \mathbf{X}^{0'}_{k,\ell}$ from $\mathbf{X}^{0'}_{k,\ell}$ to $\mathbf{X}^0$
               (see Figure 5b) and obtain $\hat{\boldsymbol{\sigma}}^0_{k,\ell}$ by means of a FE simulation.
    END FOR
             $\hat{\boldsymbol{\sigma}}^0_k \leftarrow \underset{\ell}{\mathrm{mean}}\,[\hat{\boldsymbol{\sigma}}^0_{k,\ell}]$
             ■ Solve Eq. (35). and obtain $\boldsymbol{\sigma}^0_{k+1}$.
             ■ Update variable $\bar{\boldsymbol{\sigma}}^0 = \boldsymbol{\sigma}^0_{k+1}$.
             ■ Obtain the new updated stress-free configuration $\bar{\mathbf{X}}^{0'}$
               through a relaxation step in a FE simulation from stressed
               $\bar{\boldsymbol{\sigma}}^0$ configuration $\mathbf{X}^0$ using incompatible mesh with duplicated nodes.
    $k \leftarrow k + 1$
END WHILE
```

4. Results and discussion

Based on this algorithm, we present results on the inverse reconstruction of variables in the reference and loaded configurations, with special emphasis to the recovery of residual stresses. First, we formulate the problem. Then, we show results using noise-free and noisy input displacement data.

4.1. Example of application: biaxially loaded sample

We consider a square sample of size $L \times L$. The sample is subjected to a nonlinear growth process in an ellipsoidal region (Figure 6a). Growth (Figure 6b) is modeled through a multiplicative deformation as defined in Figure 2. Once a deformed (reference) configuration is obtained after growth, the sample is biaxially loaded (Figure 6a) by means of FE simulations (mesh shown in Figure 6c), The biaxial (virtual) sample is loaded along the boundaries using rigid grips, and the overall force and deformation along the two axis (vertical and horizontal) are recorded for different load cases (Figure 6d).

Under the hypothesis that the real biaxial device, load cells and grip motion are well calibrated and aligned, we assume that noise-free overall forces and deformations are obtained in the experiments for all the load cases. Overall forces and deformations $F_X|_\ell, U_X|_\ell, F_Y|_\ell, U_Y|_\ell$ (Figure 6a) for the different load cases ℓ are one of the input data in our algorithm, as can be seen in Eqs. (28)-(29). Similarly, we generate discrete displacement fields $\mathbf{u}_\ell^{E\star}$ in the sample domain for each loading cases ℓ which make the second stack of input data according to Eqs. (26–27). These displacement fields are synthetically generated via FE simulations and these are considered the ground truth solution. Using this noise-free ground truth displacements first, and then adding Gaussian noise; residual stress, displacement and strain fields are reconstructed and shown in next sections. All the FE simulations were performed using the mesh shown in Figure 6c.

4.2. Noise-free displacement input data

The growth problem illustrated in the square sample of Figure 6a is subjected to biaxial loading from the reference configuration, following growth, as depicted for load case 1 in Figure 6d. The various components of the residual stress tensor in the reference configuration, along with the components of the displacement field and the logarithmic strain tensor in the loaded configuration, are shown in Figure 7. These results serve as the ground truth solution for the specified load case 1.

The residual stress tensor in the reference configuration, along with the displacement field and logarithmic strain tensor in the loaded configuration, are subsequently reconstructed. The quantities F_X, U_X, F_Y, and U_Y obtained from the biaxial test, as well as the noise-free (ground truth) displacement

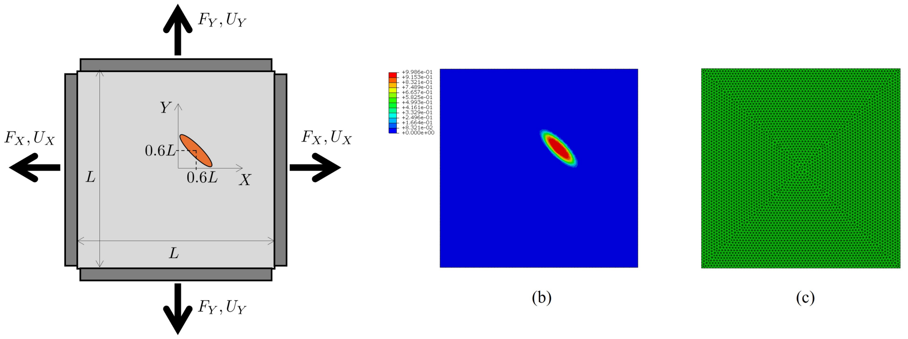

(a) (b) (c)

LC	1	2	3	4	5	6	7	8	9	10	11	12	13	14	15	16
U_x/L	0.1	0.15	0.2	0.25	0.1	0.15	0.2	0.25	0.1	0.15	0.2	0.25	0.1	0.15	0.2	0.25
U_Y/L	0.1	0.1	0.1	0.1	0.15	0.15	0.15	0.15	0.2	0.2	0.2	0.2	0.25	0.25	0.25	0.25

(d)

Figure 6: Example of application for the inverse algorithm. (a) Biaxially loaded sample as an example for inverse recovery of residual stress, displacement and strain fields. A growth process is produced at the ellipsoidal location marked with orange color. Growth is modeled analogously to the example shown in Figure 2. (b) Values of γ (Figure 2) of the deformation gradient in the sample. (c) FE mesh used in the different simulations. (d) 2-axis deformations applied through the grips (considered as rigid) for the different load cases (LC).

field for load case 1, are used as input data for our inverse algorithm. The results of this noise-free inverse solution are presented in Figure 7. A perfect recovery of the variables compared to their ground truth counterparts is observed, demonstrating the accuracy of our inverse approach.

4.3. Noisy displacement input data

In this case, the input quantities of the inverse algorithm obtained in the biaxial test are F_X, U_X, F_Y, U_Y t, and the noisy displacement fields for different load cases. Noisy displacement field are generated by adding Gaussian noise to the ground truth solution for each load case as follows,

$$\mathbf{u}_k^{E\star} = \mathbf{u}_k^{E,GT} + \boldsymbol{\xi} \cdot \left\| \mathbf{u}_k^{E,GT} \right\| / \left\| \mathbf{u}_1^{E,GT} \right\| \tag{36}$$

where $\mathbf{u}_k^{E\star}$ and $\mathbf{u}_k^{E,GT}$ are the noisy and ground truth displacement vectors, respectively, that contain the different components of the displacement field at each node of the FE mesh for each load case k. The random-valued vector

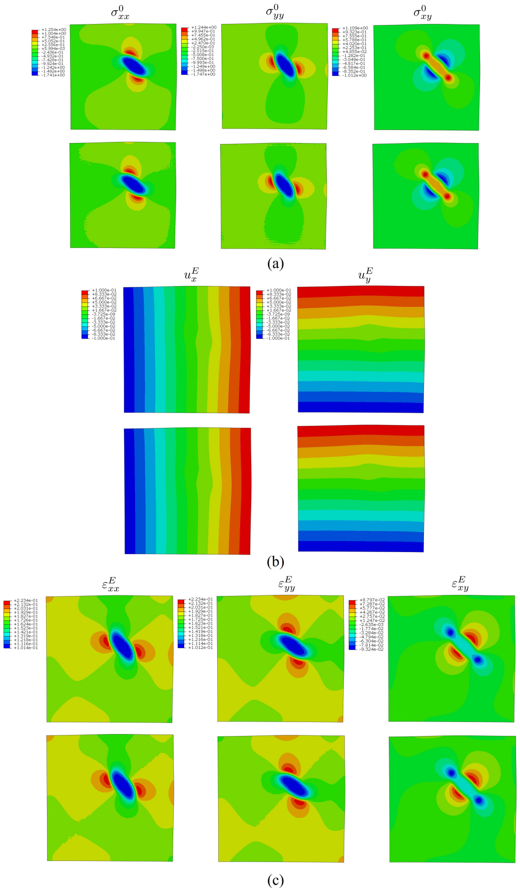

Figure 7: Ground truth and noise-free inverse reconstructed quantities by the inverse algorithm for the example of application shown in Figure 6. (a) Dimensionless components (over E) of the Cauchy's residual stress tensor in the reference configuration. First row: ground-truth solution. Second row: reconstructed solution by the inverse algorithm. (b) Dimensionless components (over L) of the displacement field in the loaded configuration of the biaxial test for the load case 1 (Figure 6). First row: ground-truth solution. Second row: reconstructed solution by the inverse algorithm. (c) Components of the logarithmic strain tensor in the loaded configuration of the biaxial test for the load case 1 (Figure 6). First row: ground-truth solution. Second row: reconstructed solution by the inverse algorithm.

$\boldsymbol{\xi}$, follows a Gaussian distribution $\mathcal{N}(0, s)$, with standard deviation s. This vector $\boldsymbol{\xi}$ is scaled for each load case k, as seen in Eq. (36), over load case 1 in order to keep similar errors versus the ground truth solution for the different load cases.

The synthetically generated noisy displacements model experimental acquisition of displacements using, for instance, DIC techniques. Two different levels of noise are considered in the study: a high noise level with parameter $s = 5 \cdot 10^{-4} \cdot L$ in the Gaussian distribution, and a low noise level with parameter $s = 2 \cdot 10^{-4} \cdot L$. Moreover, we define the following error metric to estimate the error of the strain field introduced by noisy displacement fields:

$$\text{Err E } (\%) = 100 \cdot \sqrt{\sum_{i=1}^{NE} \frac{\left(\varepsilon_{xx,i}^{E,GT} - \varepsilon_{xx,i}^{E\star}\right)^2 + \left(\varepsilon_{yy,i}^{E,GT} - \varepsilon_{yy,i}^{E\star}\right)^2 + \left(\varepsilon_{xy,i}^{E,GT} - \varepsilon_{xy,i}^{E\star}\right)^2}{\left(\varepsilon_{xx,i}^{E,GT}\right)^2 + \left(\varepsilon_{yy,i}^{E,GT}\right)^2 + \left(\varepsilon_{xy,i}^{E,GT}\right)^2}}, \tag{37}$$

where $\varepsilon_{xx,i}^{E,GT}$, $\varepsilon_{yy,i}^{E,GT}$, $\varepsilon_{xy,i}^{E,GT}$ and $\varepsilon_{xx,i}^{E\star}$, $\varepsilon_{yy,i}^{E\star}$, $\varepsilon_{xy,i}^{E\star}$ are the components of the logarithmic strain tensor at each element i, derived from the ground truth and noisy displacement fields, respectively. NE is the number of elements of the FE mesh.

Figure 8a shows the input noisy displacement field, and corresponding strain tensor fields (Figure 8b) for load case 1 (see Figure 6) and the different noise levels. Moreover, the errors introduced in the strain field by noise in the displacement field, computed according Eq. (37), are shown in Figure 8c for each load case. The mean errors in the strain field for all the load cases is set to 29.4 (%) for the high noise level and to 11.7 (%) for the low noise level.

Figures 9 and 10 present the reconstructed residual stress fields in the reference configuration for high and low noise levels, respectively. The reconstruction used varying numbers of input data stacks corresponding to different load cases. For comparison, the ground truth solution is included in both figures. It is clear that the reconstructed residual stress fields converge toward the ground truth solution as the number of load cases in the biaxial tests—and consequently the number of input data stacks—increases. This trend is consistent across both noise levels and can be interpreted similarly to machine learning techniques, where expanding the data (training) space improves the solution quality.

As expected, the reconstructions are more accurate in the low-noise scenario. Overall, the reconstructed residual stress fields shown in Figures 9 and 10 are qualitatively robust across all noise levels and input data config-

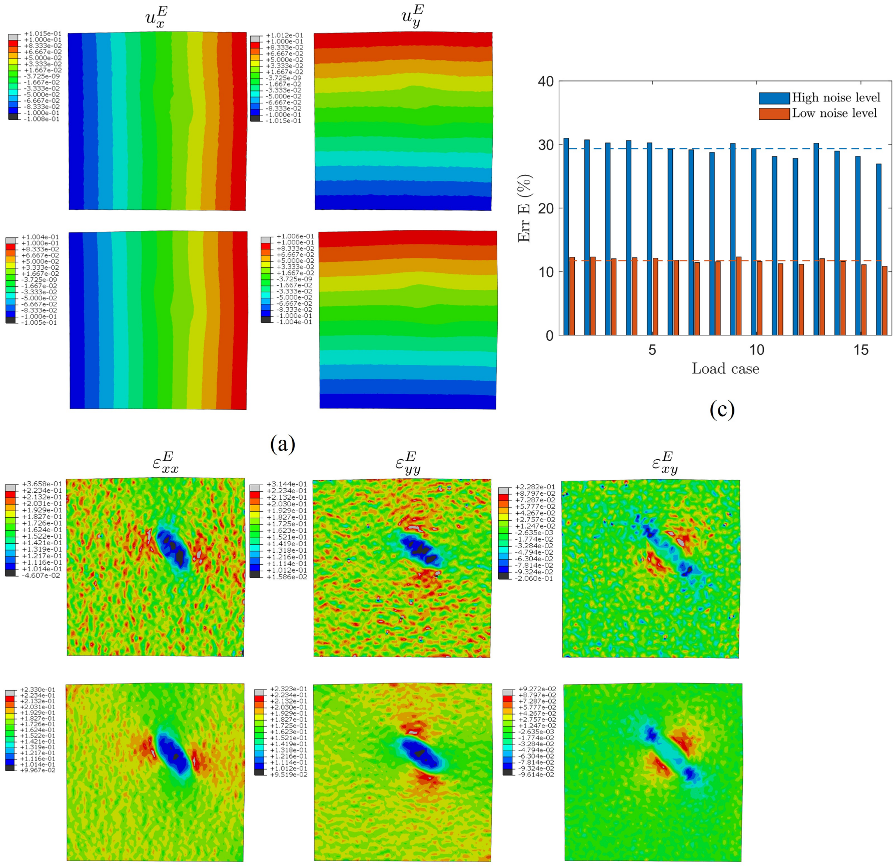

(a)

(c)

(b)

Figure 8: Generated noisy input data for the inverse algorithm. (a) Dimensionless components (over L) of the displacement field in the loaded configuration of the biaxial test for the load case 1 (Figure 6). First row: high noise level case. Second row: low noise level case. (b) Corresponding components of the logarithmic strain tensor in the loaded configuration of the biaxial test for the load case 1 (Figure 6). First row: high noise level case. Second row: low noise level case. (c) Errors introduced in the logarithmic strain field by added noise in the displacement field, computed according Eq. (37), for each load case. Mean values are represented by dashed lines for each noise level.

urations. Notably, excellent results are achieved when more than one stack of data (load case) is used for reconstruction.

In order to quantify the error of the residual stress fields for the different

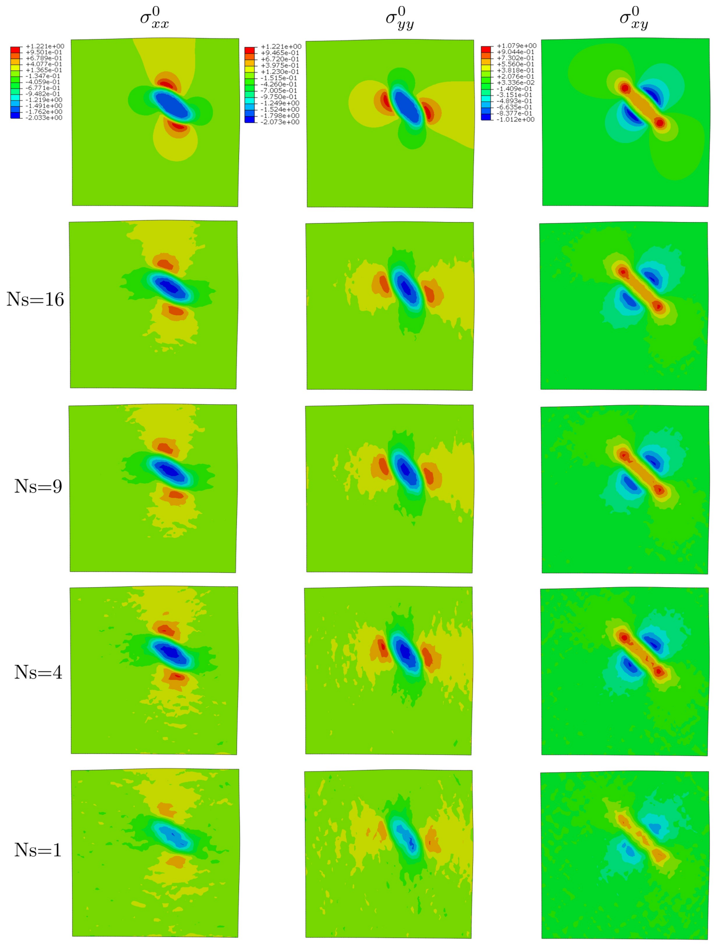

Figure 9: Dimensionless components (over E) of the Cauchy's residual stress tensor in the reference configuration. Different load cases, and hence different number of stacks (Ns) of noisy input displacement data (high noise level) were used for reconstruction. Load case 1 was used for Ns=1; load cases 1, 4, 13 and 16 were used for Ns=4; load cases 1, 3, 4, 9, 11, 12, 13, 15 and 16 were used for Ns=9; all load cases were used for Ns=16 (see Figure 6d). The first row represents the ground truth solution for comparison purposes. Regularization parameter $\lambda = 5 \cdot 10^{-5}$ (dimensionless value) according to the L-curve of Figure S1.

cases considered in Figures 9 and 10, the following metric is introduced:

$$\text{Err S }(\%) = 100 \cdot \sqrt{\sum_{i=1}^{NE} \frac{\left(\sigma^{0,GT}_{xx,i} - \sigma^{0}_{xx,i}\right)^2 + \left(\sigma^{0,GT}_{yy,i} - \sigma^{0}_{yy,i}\right)^2 + \left(\sigma^{0,GT}_{xy,i} - \sigma^{0}_{xy,i}\right)^2}{\left(\sigma^{0,GT}_{xx,i}\right)^2 + \left(\sigma^{0,GT}_{yy,i}\right)^2 + \left(\sigma^{0,GT}_{xy,i}\right)^2}}, \tag{38}$$

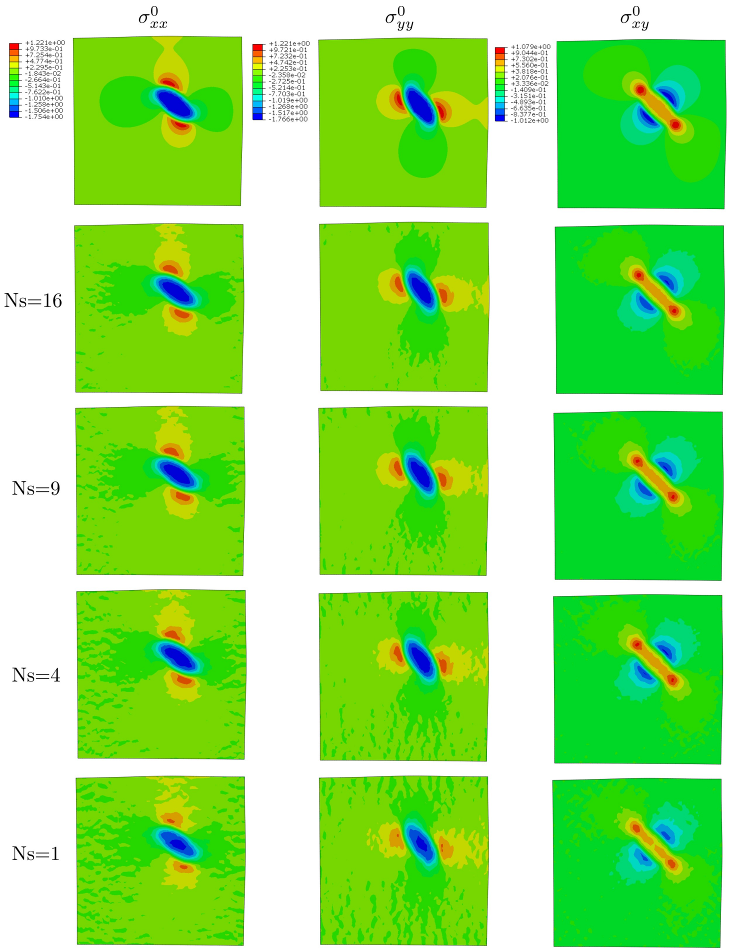

Figure 10: Dimensionless components (over E) of the Cauchy's residual stress tensor in the reference configuration. Different load cases, and hence different number of stacks (Ns) of noisy input displacement data (low noise level) were used for reconstruction. Load case 1 was used for Ns=1; load cases 1, 4, 13 and 16 were used for Ns=4; load cases 1, 3, 4, 9, 11, 12, 13, 15 and 16 were used for Ns=9; all load cases were used for Ns=16 (see Figure 6d). The first row represents the ground truth solution for comparison purposes. Regularization parameter $\lambda = 2 \cdot 10^{-5}$ (dimensionless value) according to the L-curve of Figure S2.

where $\sigma^{0,GT}_{xx,i}$, $\sigma^{0,GT}_{yy,i}$, $\sigma^{0,GT}_{xy,i}$ and $\sigma^0_{xx,i}$, $\sigma^0_{yy,i}$, $\sigma^0_{xy,i}$ are the components of the Cauchy's residual stress at each element i, of the ground truth and recovered from noisy displacement fields, respectively; and NE is the number of elements in the

FE mesh. The errors of the recovered stress fields from noisy displacement fields, computed according Eq. (38), are shown in Figure 11 for each noise level and stacks (load cases) used for reconstruction. As observed in Figures 9 and 10, the error in the reconstruction is always lower for the low noise level case with a rapid decay as the number of stacks used for reconstruction increases. The lowest errors are achieved when all the load cases in the biaxial test are considered ($Ns = 16$), being 17.8% for the high noise level and to 12.8% for the low noise level for the defined error metric. Regardless of these values, residual stress reconstructions considering all load cases show a very good agreement against the ground truth solution as shown Figures 9 and 10.

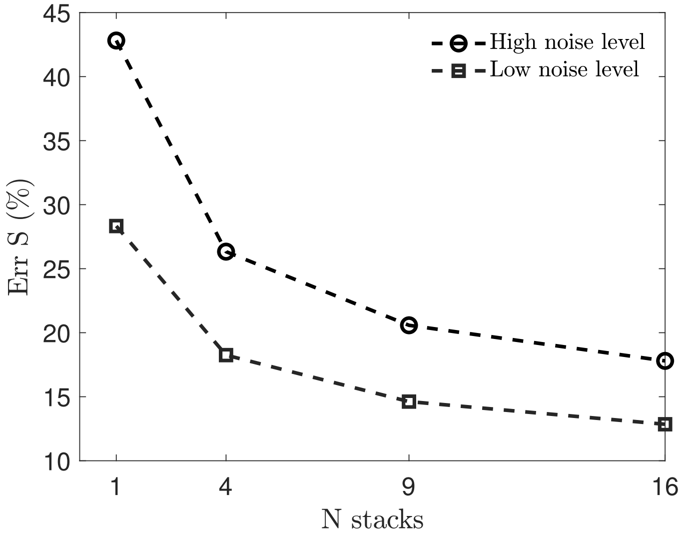

Figure 11: Errors of the recovered residual stress fields from noisy the displacement fields, computed according Eq. (38), for each noise level and stacks (load cases) used as input data for reconstruction.

Although the present study is focused on the recovery of residual stress patterns, results regarding reconstruction of elastic displacements and corresponding strain fields are also of interest as part of the developed methodology. In this sense, Figures 12 and 13 show the recovered elastic strain fields in the loaded configuration for the high and low noise levels, respectively. Results are presented just for the first load case (see Figure 6d), and analogously to the residual stress, results are shown for different number of stacks of input data, corresponding to different load cases. The ground truth solution is included in Figures 12 and 13 for comparison purposes. Again, we observe the same improvement and quality of reconstruction of the strain fields with the number of stacks and noise levels. The errors of the recovered strain fields from noisy displacement fields versus the ground truth solution, computed using recovered strain fields in Eq. (37) instead of noisy fields, are shown in Figure 14a (high noise level) for all the considered stacks used for reconstruction and corresponding load cases (see Figure 6d), and in Figure 14b for the low noise level case. As in the case of reconstructed residual stress patterns, the error in strain reconstruction shows a rapid decay as the number of stacks used for reconstruction increases, being always lower for the low noise level as expected. According to the errors shown in Figure 14, the quality of the recovered elastic strain field is very good for all the cases considered. Moreover, we observe a significant improvement of the recovered strain fields and errors in Figures 12, 13 and 14 versus the input strain fields and errors shown in Figure 8. We also observe in Figure 14 no significant differences in the quality of reconstructed strain fields with specific load cases.

The recovered stress fields in Figures 9 and 10 assume that the mechanical characteristics of the specimen, i.e. constitutive law and associated parameters, are known a priori and retained during the growth process, as is usually assumed in the growth modeling literature. Although this hypothesis can be justified in a number of relevant physiological processes and diseases, growth of pathological tissues (e.g. malignant tumors) may induce both residual stresses and tissue stiffness heterogeneity. This is clearly a limitation of our work. In this context, the proposed mathematical approach can be complemented with elastography inverse formulations [57–60] to get both stiffness and residual stress maps. This issue will be investigated in future work. Nevertheless, as pointed out before, the present inverse approach is independent from the origin of the residual stresses. Therefore, this framework can be applied beyond growth problems in which this limitation does not hold to recover, for instance, active stress fields present in tissues as a consequence of cells' activity, or the active component of engineering materials (e.g. electroactive, liquid crystal elastomers,...).

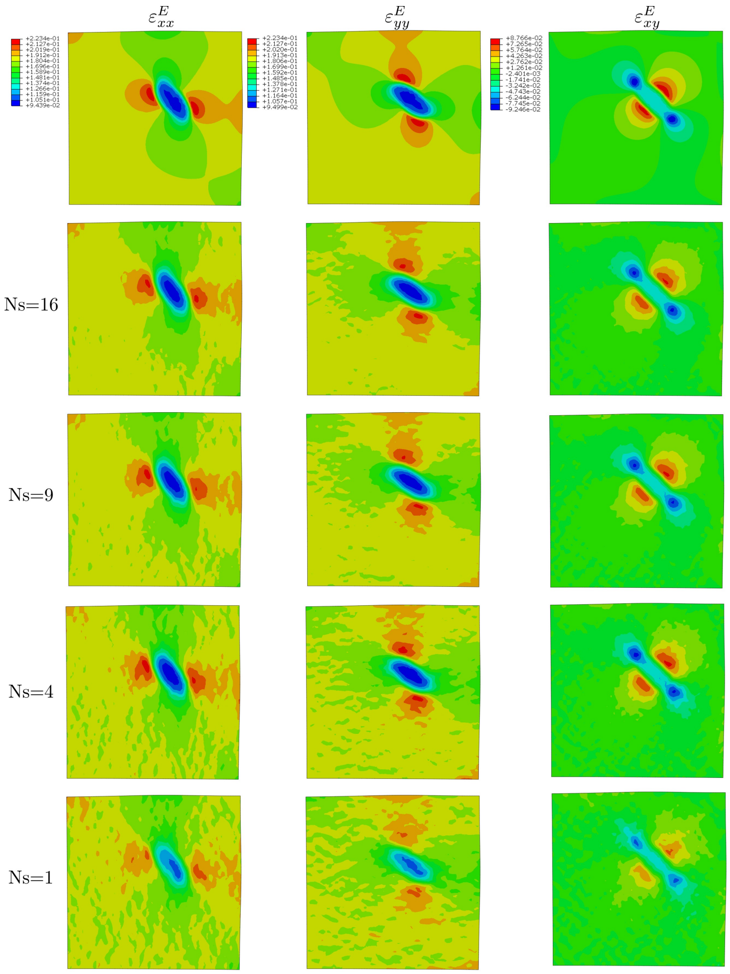

Figure 12: Components of the logarithmic strain tensor in the loaded configuration presented for the first load case (see Figure 6d). Different load cases, and hence different number of stacks (Ns) of noisy input displacement data (high noise level) were used for reconstruction. Load case 1 was used for Ns=1; load cases 1, 4, 13 and 16 were used for Ns=4; load cases 1, 3, 4, 9, 11, 12, 13, 15 and 16 were used for Ns=9; all load cases were used for Ns=16 (see Figure 6d). The first row is the ground truth solution, shown for comparison purposes.

5. Conclusion

In this study, we developed and introduced a novel inverse approach for quantifying complex residual stress patterns within a nonlinear continuum

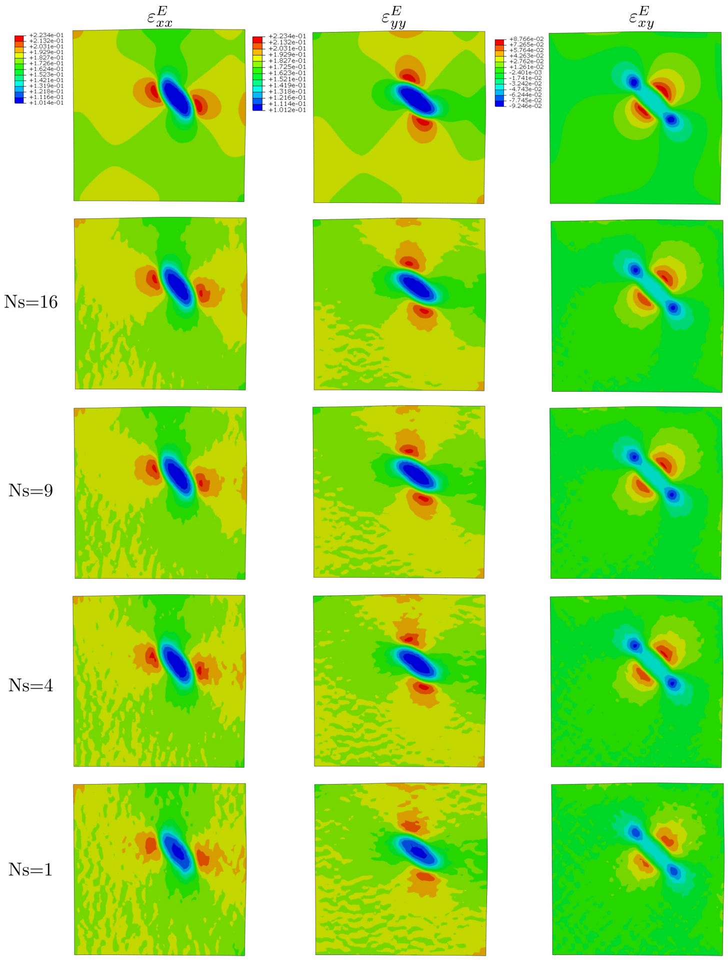

Figure 13: Components of the logarithmic strain tensor in the loaded configuration presented for the first load case (see Figure 6d). Different load cases, and different number of stacks (Ns) of noisy input displacement data (low noise level) were used for reconstruction. Load case 1 was used for Ns=1; load cases 1, 4, 13 and 16 were used for Ns=4; load cases 1, 3, 4, 9, 11, 12, 13, 15 and 16 were used for Ns=9; all load cases were used for Ns=16 (see Figure 6d). The first row is the ground truth solution, shown for comparison purposes.

framework. The methodology demonstrated the feasibility of recovering these stresses using an externally loaded configuration, leveraging the distinct displacement fields arising from material nonlinearity when the reference configuration is prestressed as opposed to stress-free. Notably, the approach is limited to solids that show a nonlinear constitutive behavior, typically found

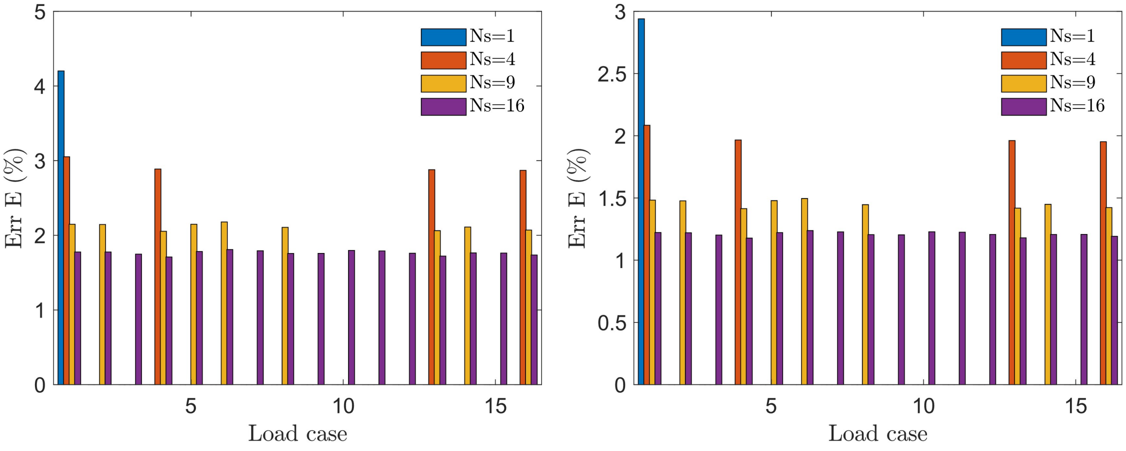

(a) (b)

Figure 14: Errors of the recovered elastic strain fields from noisy the displacement fields versus the ground truth solution, computed using recovered strain fields in Eq. (37) instead of noisy fields, for the different stacks (and corresponding load cases) used as input data for reconstruction. (a) High level of noise. (b) Low level of noise.

in biological materials, and the accuracy of the reconstructed stress fields may depend on the characteristics of the nonlinear constitutive law, an aspect that will be investigated in future work. Moreover, model parameters of the selected constitutive law (assumed as homogeneous) have to be calibrated a priori. However, the proposed methodology may be combined with elastography inverse formulations to get both residual stress and stiffness distributions, which may have potential interest in prestressed heterogeneous tissues.

The proposed approach relies on input experimental data and leverages external loads and domain displacement fields obtained from biaxial testing. However, the formulation can be readily adapted to accommodate other loading conditions. While this study was conducted in a theoretical context using synthetically generated data instead of experimental measurements, the required data can be experimentally acquired through mechanical testing combined with digital image correlation (DIC) methodologies.

Furthermore, the study demonstrated significant improvements in the recovery of variables when the data space was expanded by incorporating multiple load cases and corresponding data stacks into the reconstruction algorithm. This observation is similar to the general trend observed in machine learning techniques, where increasing the diversity of input data enhances solution accuracy.

While the study focused on recovering residual stresses in tissues, the framework is versatile and can be extended to explore active stresses in cells or tissues, engineered active materials, and the reconstruction of pre-stresses in various applications across industry and biology.

Acknowledgements

J.A.S.–H. was supported by the Salvador de Madariaga sabbatical fellowship of the Ministerio de Ciencia, Innovación y Universidades, grant number PRX22/00365, and MCIN/AEI/10.13039/501100011033 [PID2021-126051OB-C42].

References

[1] Goriely A (2017). The mathematics and mechanics of biological growth ,Springer.

[2] Aben, H and Anton, J and Õis, M and Viswanathan, K and Chandrasekar, S and Chaudhri, MM (2016). On the extraordinary strength of Prince Rupert's drops. Applied Physics Letters. 109: 231903.

[3] Leggatt RH (2008). Residual stresses in welded structures. International Journal of Pressure Vessels and Piping 85:144–151.

[4] Chen C, Yin J, Zhu H, Xiao Z, Zhang L, Zeng X (2019). Effect of overlap rate and pattern on residual stress in selective laser melting. International Journal of Machine Tools and Manufacture 145:103433.

[5] Xiao Z, Chen C, Zhu H, Hua Z, Nagarajan B, Guo L, Zeng X (2020). Study of residual stress in selective laser melting of Ti6Al4V. Materials and Design 193:108846.

[6] James MN, Hughes DJ, Chen Z, Lombard H, Hattingh DG, Asquith D, Yates JR, Webster PJ (2007). Residual stresses and fatigue performance. Engineering Failure Analysis 14:384–395.

[7] Barsoum Z, Barsoum I (2009). Residual stress effects on fatigue life of welded structures using LEFM. Engineering Failure Analysis 16:449–467.

[8] Chuong, CJ and Fung, YC (1986). Residual stress in arteries. Frontiers in biomechanics (Springer), 117–129.

[9] Guillou A, Ogden RW: Growth in soft biological tissue and residual stress development, in Mechanics of Biological Tissue, Proceedings of the IUTAM Symposium Graz 2004, 47–62, Springer (2006)

[10] Kuhl E (2014). Growing matter: a review of growth in living systems. Journal of the Mechanical Behavior of Biomedical Materials 29: 529–543.

[11] Ambrosi D, Ateshian GA, Arruda EM, Cowin SC, Dumais J, Goriely A, Holzapfel GA, Humphrey JD, Kemkemer R, Kuhl E, Olberding JE, Taber LA, Garikipati K (2011). Perspectives on biological growth and remodeling. J. Mech. Phys. Solids 59:863–883.

[12] Ambrosi D, Ben Amar M, Cyron CJ, DeSimone A, Goriely A, Humphrey JD, Kuhl E (2019). Growth and remodelling of living tissues: perspectives, challenges and opportunities. J. R. Soc. Interface 16:20190233.

[13] Dunlop JWC, Fischer FD, Gamsjäger E, Fratzl P (2010). A theoretical model for tissue growth in confined geometries. J. Mech. Phys. Solids 58:1073–1087.

[14] Epstein M, Maugin GA (2000). Thermomechanics of volumetric growth in uniform bodies. Int. J. Plast. 16:951–978.

[15] Goriely A, BenAmar M (2007). On the definition and modeling of incremental, cumulative, and continuous growth laws in morphoelasticity. Biomech. Mod. Mechanobiol. 6:289–296.

[16] Lubarda A, Hoger A (2002). On the mechanics of solids with a growing mass. Int. J. Solids Struct. 39:4627–4664.

[17] Socci L, Rennati G, Gervaso F, Vena P (2007). An axisymmetric computational model of skin expansion and growth. Biomech. Model. Mechanobiol. 6:177–188.

[18] Tepole AB, Ploch CJ, Wong J, Gosain AK, Kuhl E (2011). Growing skin: a computational model for skin expansion in reconstructive surgery. J. Mech. Phys. Solids 59:2177–2190.

[19] Ambrosi D, Mollica F (2002). On the mechanics of a growing tumor. Int. J. Eng. Sci. 40:1297–1316.

[20] Dervaux J, Ben Amar M (2011). Buckling consideration in constrained growth. J. Mech. Phys. Solids 59:538–560.

[21] Ballatore F, Lucci G, Giverso C (2024). Modelling and simulation of anisotropic growth in brain tumours through poroelasticity: A study of ventricular compression and therapeutic protocols. Computational Mechanics 74:1137–1169.

[22] Li B, Cao YP, Feng XQ, Gao H (2011). Surface wrinkling of mucosa induced by volumetric growth: Theory, simulation and experiment. J. Mech. Phys. Solids 59:758–774.

[23] Moulton DE, Goriely A (2011). Circumferential buckling instability of a growing cylindrical tube. J. Mech. Phys. Solids 59:525–537.

[24] Rausch MK, Kuhl E (2013) On the effect of prestrain and residual stress in thin biological membranes. J. Mech. Phys. Solids 61:1955–1969.

[25] Garikipati K, Arruda EM, Grosh K, Narayanan H, Calve S (2004). A continuum treatment of growth in biological tissue: The coupling of mass transport and mechanics. J. Mech. Phys. Solids 52:1595–1625.

[26] Peña E, Calvo B, Martinez MA, Doblare M (2006). A three-dimensional finite element analysis of the combined behavior of ligaments and menisci in the healthy human knee joint. Journal of biomechanics 39:1686–1701.

[27] Budday S, Steinmann P, Kuhl E (2014). The role of mechanics during brain development. J. Mech. Phys. Solids 72:75–92.

[28] Budday S (2023). Exploring human brain mechanics by combining experiments, modeling, and simulation. Brain Multiphysics 5:100076.

[29] Budday S, Raybaud C, Kuhl E (2014). A mechanical model predicts morphological abnormalities in the developing human brain. Scientific Reports 4:5644.

[30] Holzapfel GA, Ogden RW (2009). Modelling the layer-specific three-dimensional residual stresses in arteries, with an application to the human aorta. J. Royal Soc. Int. 7:787–799.

[31] Humphrey J (2002). Cardiovascular tissue mechanics: Cells, tissues, and organs. Springer. 2002

[32] Kuhl E, Maas R, Himpel G, Menzel A (2007). Computational modeling of arterial wall growth: Attempts towards patient-specific simulations based on computer tomography. Biomech. Mod. Mechanobiol. 6:321–331.

[33] Taber LA, Humphrey JD (2001). Stress-modulated growth, residual stress, and vascular heterogeneity. J. Biomech. Eng. 123:528–535.

[34] Zhang W, Sommer G, Niestrawska JA, Holzapfel GA, Nordsletten D (2022). The effects of viscoelasticity on residual strain in aortic soft tissues. Acta Biomaterialia 140:398–411.

[35] Humphrey JD, Schwartz MA (2021). Vascular Mechanobiology: Homeostasis, Adaptation, and Disease. Annual Review of Biomedical Engineering 23, 1–27.

[36] Göktepe S, Abilez OJ, Parker KK, Kuhl E (2010). A multiscale model for eccentric and concentric cardiac growth through sarcomerogenesis. J. Theor Biol. 265:433–442.

[37] Kroon W, Delhaas T, Arts T, Bovendeerd P (2009). Computational modeling of volumetric soft tissue growth: Application to the cardiac left ventricle. Biomech. Model. Mechanobiol. 8:310–309.

[38] Rausch MK, Dam A, Göktepe S, Abilez OJ, Kuhl E (2011). Computational modeling of growth: Systemic and pulmonary hypertension in the heart. Biomech. Model. Mechanobiol. 10:799–811.

[39] Cilla M, Peña E, Martinez MA (2012). 3D computational parametric analysis of eccentric atheroma plaque: influence of axial and circumferential residual stresses. Biomech. Model. Mechanobiol. 11:1001–1013.

[40] Horvat N, Virag L, Holzapfel GA, Soric J, Karšaj I (2019) A finite element implementation of a growth and remodeling model for soft biological tissues: verification and application to abdominal aortic aneurysms. Comput. Methods Appl. Mech. Eng. 352:586–605.

[41] Saez P, Peña E, Martinez MA, Kuhl E (2014). Computational modeling of hypertensive growth in the human carotid artery. Comput. Mech. 53:1183–1196.

[42] Reina-Romo E, Gomez-Benito MJ, Garcia-Aznar JM, Dominguez J, Doblare M (2010). Growth mixture model of distraction osteogenesis: effect of pre-traction stresses. Biomech. Model. Mechanobiol. 9:103–115.

[43] Fung YC, Liu SQ (1989). Change of residual strains in arteries due to hypertrophy caused by aortic constriction. Circ. Res.65:1340–1349.

[44] Fung YC (1991). What are the residual stresses doing in our blood vessels. Ann. Biomed. Eng. 19:237–249.

[45] Holzapfel GA, Sommer G, Auer M, Regitnig P, Ogden RW (2007). Layer-specific 3D residual deformations of human aortas with non-atherosclerotic intimal thickening. Ann. Biomed. Eng. 35:530–545.

[46] Garcia-Herrera CM, Bustos CA, Celentano DJ, Ortega R (2016). Mechanical analysis of the ring opening test applied to human ascending aortas. Comput. Methods Biomech. Biomed. Engin. 19:1738–1748.

[47] Peña JA, Martinez MA, Peña E (2015). Layer-specific residual deformations and uniaxial and biaxial mechanical properties of thoracic porcine aorta. J. Mech. Behav. Biomed. Mater. 50:55–69.

[48] Diaz C, Peña JA, Martinez MA, Peña E (2021). Unraveling the multilayer mechanical response of aorta using layer-specific residual stresses and experimental properties J. Mech. Behav. Biomed. Mater. 113:104070

[49] Legant WR, Miller JS, Blakely BL, Cohen DM, Genin GM, Chen CS (2010). Measurement of mechanical tractions exerted by cells in three dimensional matrices. Nature Methods 7:969–971.

[50] Michel R, Peschetola V, Vitale G, Etienne J, Duperray A, Ambrosi D, Preziosi L, Verdier C (2013). Mathematical framework for traction force microscopy. ESAIM: Proc. 42:61–83.

[51] Song D, Dong L, Gupta M, Li L, Klaas O, Loghin A, Beall M, Chen CS, Oberai AA (2020). Recovery of tractions exerted by single cells in three dimensional nonlinear matrices. Journal of Biomechanical Engineering 142.

[52] Sanz-Herrera JA, Barrasa-Fano J, Condor M, Van Oosterwyck H (2021). Inverse method based on 3D nonlinear physically constrained minimisation in the framework of traction force microscopy. Soft Matter 17:10210–10222.

[53] Barrasa-Fano J, Shapeti A, de Jong J, Ranga A, Sanz-Herrera JA, Van Oosterwyck H (2021). Advanced in silico validation framework for three dimensional traction force microscopy and application to an in vitro model of sprouting angiogenesis, Acta Biomaterialia 126:326–338.

[54] Apolinar-Fernandez A, Barrasa-Fano J, Condor M, Van Oosterwyck H, Sanz-Herrera JA (2023). Traction force reconstruction assessment on real three dimensional matrices and cellular morphologies. International Journal of Engineering Science 186:103828.

[55] Apolinar-Fernandez A, Barrasa-Fano J, Van Oosterwyck H, Sanz-Herrera JA (2024). Multiphysics modeling of 3d traction force microscopy with application to cancer cell-induced degradation of the extracellular matrix. Engineering with Computers (2024).

[56] Song D, Seidl DT, Oberai AA (2020). Three-dimensional traction microscopy accounting for cell-induced matrix degradation. Computer Methods in Applied Mechanics and Engineering 364:112935.

[57] Goenezen A, Barbone P, Oberai AA (2011). Solution of the nonlinear elasticity imaging inverse problem: The incompressible case. Comput. Methods Appl. Mech. Engrg. 200:1406–1420.

[58] Canovic EP, Thomas Seidl D, Polio SR, Oberai AA, Barbone PE, Stamenovic D, Smith ML (2014). Biomechanical imaging of cell stiffness and prestress with subcellular resolution Biomech Model Mechanobiol 13:665–678.

[59] Chen S, Xu W, Kim J, Nan H, Zheng Y, Sun B, Jiao Y (2019). Novel inverse finite-element formulation for reconstruction of relative local stiffness in heterogeneous extra-cellular matrix and traction forces on active cells. Phys. Biol. 16 036002

[60] Mei Y, Feng X, Jin Y, Kang R, Wang X, Zhao D, Ghosh S, Neu CP, Avril S (2023), Cell nucleus elastography with the adjoint-based inverse solver. Computer Methods and Programs in Biomedicine 242:107827.

[61] Schwarz US, Soine JRD (2015). Traction force microscopy on soft elastic substrates: A guide to recent computational advances, Biochimica et Biophysica Acta - Molecular Cell Research 1853:3095–3104.

[62] Apolinar-Fernandez A, Blazquez-Carmona P, Ruiz-Mateos R, Barrasa-Fano J, Van Oosterwyck H, Reina-Romo E, Sanz-Herrera JA (2024). Regularization techniques and inverse approaches in 3D Traction Force Microscopy. International Journal of Mechanical Sciences 283:109592.

[63] Peña JA, Corral V, Martinez MA, Peña E (2018). Over length quantification of the multiaxial mechanical properties of the ascending, descending and abdominal aorta using Digital Image Correlation. J. Mech. Behav. Biomed. Mater. 77:434–445.

[64] Maiti R, Gerhardt L-C, Lee ZS, Byers RA, Woods D, Sanz-Herrera JA, Franklin SE, Lewis R, Matcher SJ, Carre MJ (2016). In vivo measurement of skin surface strain and sub-surface layer deformation induced by natural tissue stretching. J. Mech. Behav. Biomed. Mater. 62:556–569.

[65] Gustafsson A, Mathavan N, Turunen MJ, Engqvist J, Khayyeri H, Hall SA, Isaksson H (2018). Linking multiscale deformation to microstructure in cortical bone using in situ loading, digital image correlation and synchrotron X-ray scattering. Acta Biomater. 69:323–331.

[66] Mora-Macias J, Ayensa-Jimenez J, Reina-Romo E, Doweidar MH, Dominguez J, Doblare M, Sanz-Herrera JA (2020). A multiscale data-driven approach for bone tissue biomechanics. Computer Methods in Applied Mechanics and Engineering 368:113136.

[67] P. Badel, K. Genovese, S. Avril (2012). 3D Residual Stress Field in Arteries: Novel Inverse Method Based on Optical Full-field Measurements. Strain 48:528–538.

[68] Vogel CR (2002). Computational methods for inverse problems. Society for Industrial and Applied Mathematics. Philadelphia, PA, USA, 2002.

[69] Holzapfel GA (2000). Nonlinear solid mechanics. A continuum approach for engineering, John Wiley & Sons, England, UK, 2000.

[70] Bonet J, Wood RD (2008). Nonlinear continuum mechanics for finite element analysis. Cambridge University Press, 2 edition, 2008.

[71] Zienkiewicz EC, Taylor RL, Zhu JZ (2005).The finite element method: Its basis and fundamentals Elsevier Butterworth-Heinemann, 2005.

[72] Byrd RH, Lu P, Nocedal J, Zhu CY (1995). A limited memory algorithm for bound constrained optimization. SIAM Journal on Scientific Computing 16:1190–1208.